Monthly Notices
of the
ROYAL ASTRONOMICAL SOCIETY

MNRAS **479,** 1055–1076 (2018)
Advance Access publication 2018 May 21

doi:10.1093/mnras/sty1344

New constraints on Lyman-α opacity with a sample of 62 quasars at $z > 5.7$

Sarah E. I. Bosman,[1,2,3★] Xiaohui Fan,[4] Linhua Jiang,[5] Sophie Reed,[1] Yoshiki Matsuoka,[6] George Becker[7] and Martin Haehnelt[1,2]

[1]*Institute of Astronomy, University of Cambridge, Madingley Road, Cambridge CB3 0HA, UK*
[2]*Kavli Institute for Cosmology, University of Cambridge, Madingley Road, Cambridge CB3 0HA, UK*
[3]*Department of Physics and Astronomy, University College London, London WC1E 6BT, UK*
[4]*Steward Observatory, University of Arizona, Tucson, AZ 85721-0065, USA*
[5]*Kavli Institute for Astronomy and Astrophysics, Peking University, Beijing 100871, China*
[6]*Research Center for Space and Cosmic Evolution, Ehime University, Matsuyama, Ehime 790-8577, Japan*
[7]*Department of Physics and Astronomy, University of California, Riverside, 900 University Avenue, Riverside, CA 92521, USA*

Accepted 2018 May 16. Received 2018 May 14; in original form 2018 February 22

ABSTRACT

We present measurements of the mean and scatter of the intergalactic medium (IGM) Lyman-α opacity at $4.9 < z < 6.1$ along the lines of sight of 62 quasars at $z_{\rm source} > 5.7$, the largest sample assembled at these redshifts to date by a factor of two. The sample size enables us to sample cosmic variance at these redshifts more robustly than ever before. The spectra used here were obtained by the Sloan Digital Sky Survey, Dark Energy Survey–VISTA Hemisphere Survey, and Subaru High-z Exploration of Low-Luminosity Quasars collaborations, drawn from the Echellette Spectrograph and Imager and X-Shooter archives, reused from previous studies or observed specifically for this work. We measure the effective optical depth of Lyman-α in bins of 10, 30, 50, and 70 cMpc h^{-1}, construct cumulative distribution functions under two treatments of upper limits on flux and explore an empirical analytic fit to residual Lyman-α transmission. We verify the consistency of our results with those of previous studies via bootstrap resampling and confirm the existence of tails towards high values in the opacity distributions, which may persist down to $z \sim 5.2$. Comparing our results with predictions from cosmological simulations, we find further strong evidence against models that include a spatially uniform ionizing background and temperature–density relation. We also compare to IGM models that include either a fluctuating ultraviolet background dominated by rare quasars or temperature fluctuations due to patchy reionization. Although both models produce better agreement with the observations, neither fully captures the observed scatter in IGM opacity. Our sample of 62 $z > 5.7$ quasar spectra opens many avenues for future study of the reionization epoch.

Key words: intergalactic medium – quasars: absorption lines – dark ages, reionization, first stars.

1 INTRODUCTION

The first billion years of the Universe are currently a frontier of late-time cosmology, both observationally and theoretically. During this stretch of time, the first stars and galaxies assembled from the primordial gas left behind by reheating, and the atomic hydrogen permeating the early Universe became ionized. This 'reionization' transition is believed to be largely completed by redshift six. The precise timing and topology of reionization are strongly influenced by the processes at work in the first galaxies and active galactic nuclei (AGNs), as well as the large-scale structure of the early intergalactic medium (IGM).

Quasars located at $z \gtrsim 6.0$ have proven to be useful tools for obtaining information about reionization due to their high intrinsic luminosities and prominent Lyman-α emission lines. These properties have yielded results on multiple fronts, from measuring the sizes of quasar proximity zones across time, which are expected to diminish with increasing IGM neutrality and decreasing quasar lifetime (e.g. Fan et al. 2006; Carilli et al. 2010; Keating et al. 2015) to

★ E-mail: s.bosman@ucl.ac.uk

constraining enrichment processes by probing the cosmic abundances of intervening metals (e.g. Ryan-Weber et al. 2009; D'Odorico et al. 2013; Becker Bolton & Lidz 2015a; Chen et al. 2016; Bosman et al. 2017). The Lyman-α forest extending bluewards of 1215 Å in the quasar rest frame is of particular interest to reionization as it traces the diffuse intergalactic gas whose ionization is sensitive to the metagalactic ultraviolet background (UVB). The Lyman-α opacity in the forest increases with redshift, and eventually complete absorption is reached once the IGM reaches average hydrogen neutral fractions of $f \geqslant 0.1$ per cent (Gunn & Peterson 1965). The characterization of Lyman-α opacity across redshift is a powerful constraint on models of reionization, as the amount of residual transmission is sensitive to the nature of the UV sources, the thermal state of the IGM, and the large-scale clustering of sources among other factors (e.g. McQuinn et al. 2011; Wyithe & Bolton 2011; Davies et al. 2017).

Lyman-α transmission along quasar lines of sight is often quantified by an 'effective optical depth', $\tau = -\ln(\langle F/F_0 \rangle)$, where F is the observed (residual) flux in the Lyman-α forest, and F_0 is the unabsorbed continuum (e.g. Fan et al. 2006). The first studies of the optical depth distribution pointed to a large scatter in transmission along lines of sight (Songaila 2004; Fan et al. 2006). Although this scatter was potentially incompatible with the predicted scatter due to large-scale fluctuations in the density field alone (Lidz Oh & Furlanetto 2006), firm conclusions were limited by the relatively modest sample sizes (e.g. Mesinger 2010). Becker et al. (2015b) discovered a $\sim$110 cMpc Lyman-α trough extending down to $z \simeq 5.5$ and demonstrated that its existence, as well as the general distribution of Lyman-α opacity measurements at $z \gtrsim 5.6$, is incompatible with a spatially uniform UVB. The discovery prompted a flurry of new reionization models (see e.g. Chardin et al. 2015; D'Aloisio et al. 2015; Davies & Furlanetto 2016). The combined samples of Fan et al. (2006) and Becker et al. (2015b) included 26 quasars at $z > 5.7$, which is only a fraction of the more than 200 quasars now known at these redshifts. In this paper, we gather 62 spectra of $z > 5.7$ quasars, more than doubling previous samples.

We present updated measurements of the Lyman-α opacity distribution function (PDF) for the redshift range $4.9 < z < 6.1$. The number of known quasars at $z > 5.9$ is increasing rapidly due to searches by the Dark Energy Survey (DES; Reed et al. 2015), the Subaru High-z Exploration of Low-Luminosity Quasars (SHELLQs; Matsuoka et al. 2016), the Panoramic Survey Telescope and Rapid Response System (Pan-STARRS, Kaiser et al. 2010), the VISTA Kilo-Degree Infrared Galaxy (Venemans et al. 2013; Carnall et al. 2015) survey, the Canada–France High-redshift Quasar Survey (CFHQS; Willott et al. 2007), and UKIRT Infrared Deep Sky Survey (UKIDSS, Venemans et al. 2007; Mortlock et al. 2009, 2011) as well as the completion of the search for high-redshift quasars in the Sloan Digital Sky Survey (SDSS, York et al. 2000, Jiang et al. 2016). Here, we take advantage of this increase to provide smoother constraints on the Lyman-α PDF with a better handle on cosmic variance. In addition, we are able to robustly sample the Lyman-α opacity distribution up to $z = 6.1$ for the first time.

The paper is structured as follows. In Section 2, we describe our sample of 62 quasars and present four previously unpublished spectra, briefly discussing the properties of our sample. Our methods for measuring Lyman-α opacity distributions are presented, and compared to previous studies in Section 3. Challenges in dealing with the wide range of spectral resolutions and signal-to-noise ratios (S/Ns) across our sample are discussed. Section 4 gives our results spanning the redshift range $4.9 < z < 6.1$ using multiple ways of accounting for the inhomogeneous quality of the data and non-detections of transmitted flux. These results are confronted with predictions from numerical models and discussed in Section 5. Section 6 introduces our empirical functional form to residual Lyman-α transmission and outlines our maximum-likelihood fitting method. We discuss implications for the process of reionization and caveats of the work in Section 7.

The results are summarized in Section 8 and extra figures, including a mosaic of the entire sample, are shown in the Appendix A. Throughout the paper, we use $(\Omega m, \Omega\Lambda, h) = (0.308, 0.692, 0.678)$ (Planck Collaboration et al. 2016) and quote comoving distances in units of Mpc h^{-1}. We explicitly distinguish in all cases between τ and $\tau_{\rm eff}$. The latter always refers to the *binned* opacity, $\tau_{\rm eff} = -\log(\langle F \rangle)$, as defined in more detail in Section 3. The binning scale is 50 cMpc h^{-1} everywhere except in Section 4.2, where we explicitly experiment with varying it. All measurements of $\tau_{\rm eff}$ obtained and used in this paper are made available online.[1]

2 DATA

Our sample consists spectra of 62 quasars at $z > 5.7$ observed over the last 11 yr. Out of these objects, 4 are discovery spectra from the SHELLQs survey, 10 were discovered by Dark Energy Survey–VISTA Hemisphere Survey (DES–VHS, out of which four are currently unpublished), 13 are SDSS discovery spectra, 13 are new reductions of archival data, 19 are adopted from previous studies on Lyman-α transmission, and 3 are new to this work. Ten different optical spectrographs were used to obtain the data: Echellette Spectrograph and Imager (ESI), X-Shooter, Gemini Multi-Object Spectrographs (GMOS), Magellan Echellette (MagE), ESO Faint Object Spectrograph and Camera (EFOSC), Faint Object Camera and Spectrograph on the Subaru telescope (FOCAS), Multiple Mirror Telescope (MMT) Red Channel Spectrograph (RCS), High Resolution Echelle Spectrometer (HIRES), Magellan Inamori Kyocera Echelle (MIKE), and Multi-Object Double Spectrographs for the Large Binocular Telescope (LBT-MODS). The following sections describe the makeup of the sample in more detail. Table 1 details the provenance of each spectrum. A mosaic of the entire sample is plotted in Appendix A.

2.1 SDSS quasars

The SDSS is a sky survey over 14 555deg^2 which provides imaging in the *ugriz* photometric bands as well as spectroscopic follow-up using a 2.5 m dedicated telescope located at Apache Point Observatory (Fukugita et al. 1996; Hogg et al. 2001). Here, we briefly outline the detection procedure of quasars in the SDSS (see Jiang et al. 2016, for a more in-depth summary). Candidates are selected in the first step as dropouts with no detections in the *ugr* photometric bands and with colours in excess of $i_{\rm AB} - z_{\rm AB} > 2.2$. After quality cuts, follow-up photometry is obtained in the near infrared (IR) and a second cut $z_{\rm AB} - J < 0.5 + 0.5\Delta_{i-z}$ is imposed (e.g. Fan et al. 1999). Alternative colour cuts are used in deeper areas of the survey near the Galactic cap (Jiang et al. 2008, 2009) and in regions scanned two or more times (Jiang et al. 2015).

Confirmation spectra of the quasar candidates are typically obtained with the RCS on the 6.5 m MMT or Double Spectrograph on the Hale 5.1m telescope (e.g. Jiang et al. 2016), and in one occasion with the LBT-MODS on Mt. Graham in south-eastern Arizona

[1] http://www.homepages.ucl.ac.uk/ ucapeib/alldata_silver.ods

Table 1. Data used in this work. References are given in the caption of Fig. 2. A dash '–' indicates the discovery spectrum is used. Question marks in quasar names indicate a quasar yet unpublished by the discovering authors.

Quasar name	z_{em}	Instrument	S/N	Survey	Notes	Discovery ref.	Spectrum ref.
J1120+0641	7.0842	X-Shooter	35.0	UKIDSS		(1)	(26)
J1205-0000	6.8	FOCAS	3.5	SHELLQs		(20)	–
J0224–4711	6.50	GMOS	6.5	DES–VHS		(2)	–
J0210–0456	6.44	ESI	5.3	CFHQS	New reduction	(3)	(32)
J2329–0301	6.43	ESI	6.5	CFHQS	New reduction	(11)	(25)
J1148+5251	6.419	HIRES	29.7	SDSS		(4)	(22)
J1152+0055	6.37	FOCAS	3.1	SHELLQs		(20)	–
J1148+0702	6.339	HIRES	3.4	SDSS		(5)	–
J0100+2802	6.30	X-Shooter	85.2	SDSS	New spectrum	(6)	This paper
J1030+0524	6.28	X-Shooter	28.0	SDSS	New reduction	(7)	(22)
J0050+3445	6.25	ESI	24.4	CFHQS		(3)	(23)
J0323–4701	6.25	EFOSC	12.5	DES–VHS		(2)	–
J0330–4025	6.25	GMOS	12.1	DES–VHS		(2)	–
J1623+3112	6.247	ESI	16.1	SDSS		(8)	(22)
J2325-????	6.23	EFOSC	1.8	DES–VHS		(24)	–
J0410–4414	6.21	GMOS	12.7	DES–VHS		(2)	–
J0227–0605	6.20	ESI	7.5	CHFQS	New reduction	(27)	(25)
J1048+4637	6.198	HIRES	29.2	SDSS		(4)	(28)
J1609+3041	6.16	MMT	6.1	SDSS		(5)	–
J2229+1457	6.15	ESI	6.0	CHFQS	New reduction	(3)	(25)
J1250+3130	6.13	ESI	26.2	SDSS	New reduction	(9)	
J0033–0125	6.13	ESI	6.1	CHFQS	New reduction	(11)	(25)
J1319+0950	6.132	X-Shooter	96.8	UKDISS/SDSS		(10)	(23)
J1509–1749	6.12	X-Shooter	88.9	CFHQS		(11)	(22)
J2315–0023	6.117	ESI	29.8	SDSS		(12)	(23)
J0454–4448	6.10	MagE	5.8	DES		(21)	–
J0109–????	6.10	EFOSC	4.2	DES–VHS		(24)	–
J2216-0016	6.10	FOCAS	2.4	SHELLQs		(20)	–
J1602+4228	6.09	MMT	33.3	SDSS	New reduction	(8)	(25)
J0303–0019	6.078	ESI	8.0	SDSS	New reduction	(12)	(32)
J0353+0104	6.072	ESI	80.7	SDSS		(12)	(23)
J2054–0005	6.062	ESI	39.5	SDSS		(12)	(23)
J1630+4012	6.058	MMT	17.0	SDSS		(4)	(22)
J1641+3755	6.04	ESI	9.0	CHFQS	New reduction	(11)	(25)
J0408–5632	6.03	EFOSC	4.3	DES–VHS		(2)	–
J1257+6349	6.02	MMT	6.1	SDSS		(13)	–
J1306+0356	6.016	X-Shooter	55.8	SDSS	New reduction	(7)	(22)
J1137+3549	6.01	ESI	31.7	SDSS	New spectrum	(9)	This paper
J2310+1855	6.003	LBT-MODS	17.9	SDSS		(5)	–
J0818+1722	6.0	HIRES	39.8	SDSS		(9)	(28)
J0131–????	6.00	EFOSC	3.9	DES–VHS		(24)	–

(Pogge et al. 2012). Additional near-IR spectra taken for some objects do not cover the range 7500–10 000 Å required for coverage of Lyman-α at $5.3 < z < 7.0$ and are not used in this work (e.g. Jiang et al. 2007, Simcoe et al. 2011).

Jiang et al. (2016) presented the 52 final quasars discovered by the SDSS, most of which are included in this work. Out of those, 29 have been re-observed since their discovery to obtain higher quality data, while 23 have not. The discovery spectra for those 13 of these objects are included in our sample. Eight of those objects were reported in Jiang et al. (2016), three objects in Jiang et al. (2015), one objects in Jiang et al. (2009), and one object in Fan et al. (2006).

2.2 DES and DES–VHS quasars

The DES covers an area of 5000 deg^2 in the Southern hemisphere in visible imaging. It employs the dedicated Dark Energy Camera on the Blanco 4 m telescope, Cerro Tololo (The Dark Energy Survey Collaboration 2005). The first high-z quasar discovered in DES was presented in Reed et al. (2015). Quasar candidates are selected using a dropout technique similar to the SDSS procedure described above, this time with the condition $i_{DES} - z_{DES} > 1.694$. In addition, the DES survey includes the Y band, allowing a more efficient removal of red dwarfs from the sample via a constraint on the quasar continuum of $z_{DES} - Y_{DES} < 0.5$. In Reed et al. (2017), eight additional quasars were detected by combining DES data with IR observations in overlapping footprint of the VHS (McMahon et al. 2013). Nine additional objects have been discovered in the same way since (Reed et al., in preparation), of which four included here.

Spectroscopic confirmation of the candidates was conducted either with the EFOSC (Buzzoni et al. 1984) or the GMOS (Hook et al. 2004), with some objects subsequently observed in higher quality with the MagE (Marshall et al. 2008). The best-quality spectrum for each of the 10 DES–VHS quasars was chosen as shown in Table 1.

Table 2. Current list of quasars, continued. Quasar names including question marks are not public yet. References: (1) Mortlock et al. (2011); (2) Reed et al. (2017); (3) Willott et al. (2010); (4) Fan et al. (2003); (5) Jiang et al. (2016); (6) Wu et al. (2015); (7) Fan et al. (2001); (8) Fan et al. (2004); (9) Fan et al. (2006); (10) Mortlock et al. (2009); (11) Willott et al. (2007); (12) Jiang et al. (2008); (13) Jiang et al. (2015); (14) Carnall et al. (2015); (15) Goto (2006); (16) Jiang et al. (2009); (17) Fan et al. (2000); (18) Wang et al. (2016); (19) Morganson et al. (2012); (20) Matsuoka et al. (2016); (21) Reed et al. (2015); (22) McGreer Mesinger & D'Odorico (2015); (23) Becker et al. (2015b); (24) Reed (in preparation); (25) KOA (2017); (26) Bosman et al. (2017); (27) Willott et al. (2009); (28) Becker et al. (2006); (29) Venemans et al. (2013); (30) X-Shooter archives; (31) Venemans et al. (2015); (32) Eilers et al. (2017).

Quasar name	z_{em}	Instrument	S/N	Survey	Notes	Discovery ref.	Spectrum ref.
J0841+2905	5.96	ESI	11.2	SDSS		(15)	(22)
J0122-????	5.96	EFOSC	3.0	DES–VHS		(24)	–
J1202–0057	5.93	FOCAS	2.2	SHELLQs		(20)	–
J0008–0626	5.929	MMT	4.4	SDSS		(13)	–
J1411+1217	5.927	ESI	15.9	SDSS		(8)	(22)
J0148+0600	5.923	X-Shooter	128.0	SDSS		(13)	(23)
J1335+3533	5.901	ESI	16.3	SDSS		(9)	(22)
J2119–0040	5.87	MMT	4.0	SDSS		(5)	–
J2307+0031	5.87	MMT	3.6	SDSS		(5)	–
J0850+3246	5.867	MMT	3.7	SDSS		(13)	–
J0203+0012	5.86	ESI	17.4	UKIDSS/SDSS		(12)	(23)
J0005–0006	5.850	ESI	28.8	SDSS	New reduction	(8)	(32)
J1243+2529	5.85	MMT	4.1	SDSS		(5)	–
J0840+5624	5.844	ESI	17.6	SDSS		(9)	(22)
J1436+5007	5.83	MMT	3.2	SDSS		(9)	–
J0239–0045	5.82	MMT	4.9	SDSS		(16)	–
J0836+0054	5.810	X-Shooter	93.4	SDSS	New reduction	(7)	(22)
J0002+2550	5.8	HIRES	71.7	SDSS		(8)	(28)
J0810+5105	5.80	MMT	10.0	SDSS		(5)	–
J1044–0125	5.782	ESI	49.2	SDSS	New reduction	(17)	(25)
J0927+2001	5.772	X-Shooter	73.7	SDSS	New spectrum	(9)	This paper
J1621+5155	5.71	MMT	10.3	SDSS		(5)	–

2.3 SHELLQs quasars

The SHELLQs (Matsuoka et al. 2016) is a new imaging survey utilizing the Hyper Suprime-Cam on the Subaru 8.2 m telescope (Miyazaki et al. 2012). A search for quasars has currently been conducted over an area of 430 deg^2. The SHELLQs project aims to obtain deeper exposures in the *grizy* bands compared to SDSS and DES, leading to the discovery of 33 faint $z > 5.7$ quasars so far (Matsuoka et al. 2016, 2017). In this work, we include four out of the first nine SHELLQs quasar spectra presented in Matsuoka et al. (2016). The confirmation spectra for these objects were taken with the FOCAS (Kashikawa et al. 2002) as described in the discovery paper.

2.4 Other quasar spectra

In this work, we re-use 20 quasar spectra presented in previous investigations of Lyman-α opacity. McGreer Mesinger & Fan (2011) and McGreer et al. (2015) conducted observations of 22 previously known quasars with the MagE, MMT, and the X-Shooter instrument on Cassegrain UT2 (Vernet et al. 2011). We are making use of nine of those observations as indicated in Table1. Similarly, Becker et al. (2015b) published spectra of seven quasars, at $5.98 < z < 6.25$, not included in a previous work by Fan et al. (2006), obtained on the ESI on the Keck II telescope (Sheinis et al. 2002), and X-Shooter on the Very Large Telescope (VLT). Three additional spectra were first presented in Becker et al. (2006). The quasars followed up in the above papers were initially discovered by various surveys including the UKIDSS (Lawrence et al. 2007), the CFHQS (Willott et al. 2007), SDSS, and Pan-STARRS (Morganson et al. 2012). In addition, we also include a 30 h X-Shooter spectrum of ULAS J1120+0641 at $z = 7.08$, first presented in Bosman et al. (2017).

2.5 New reductions

After a proprietary period of 18 months, raw data obtained with ESI are made publicly available through the Keck Observatory Archive (KOA[2]). In this work, we use seven ESI spectra of quasars at $5.85 < z < 6.43$ rereduced from raw data obtained from the KOA. Our ESI reduction pipeline is the same as described in Section 2.6.

Finally, we rereduced the spectra of five quasars which have been previously published. X-Shooter spectra of the quasars J0836+0054 and J1030+0524 were introduced in McGreer et al. (2015), but here we use our own reduction of the raw X-Shooter files instead, in an attempt to improve data quality. ESI spectra of quasars J0210−0459, J0303−0019, and J0005−0006 were part of an observing run (PID: C197E; PI: Sargent) in 2010 October and have been previously used in e.g. Eilers et al. (2017). Here, we use our own reductions of the raw ESI data.

2.6 New spectra

We present three new observations of quasars which were carried out on the ESI, X-Shooter, and EFOSC instruments as detailed in Table 3. The spectra are plotted in Fig. 1.

An X-Shooter spectrum was obtained in 2010 January of quasar SDSS J0927+2001 at $z = 5.772$ and had not previously been published. The reduction procedure is the same as the one presented

[2]https://koa.ipac.caltech.edu/cgi-bin/KOA/nph-KOAlogin

Table 3. New observations of four $z > 5.7$ quasars which are were not presented in previous work.

Object	z	Instrument	Date	Exposure time (s)	Slit width (arcsec)	Seeing (arcsec)
SDSS J0100+2302	6.3	X-Shooter	2015 Oct 23	1800	1.00	0.80
SDSS J1137+3549	6.01	ESI	2016 Mar 18	3000	1.00	0.80
SDSS J0927+2001	5.772	X-Shooter	2010 Jan 13	1800	1.00	0.77

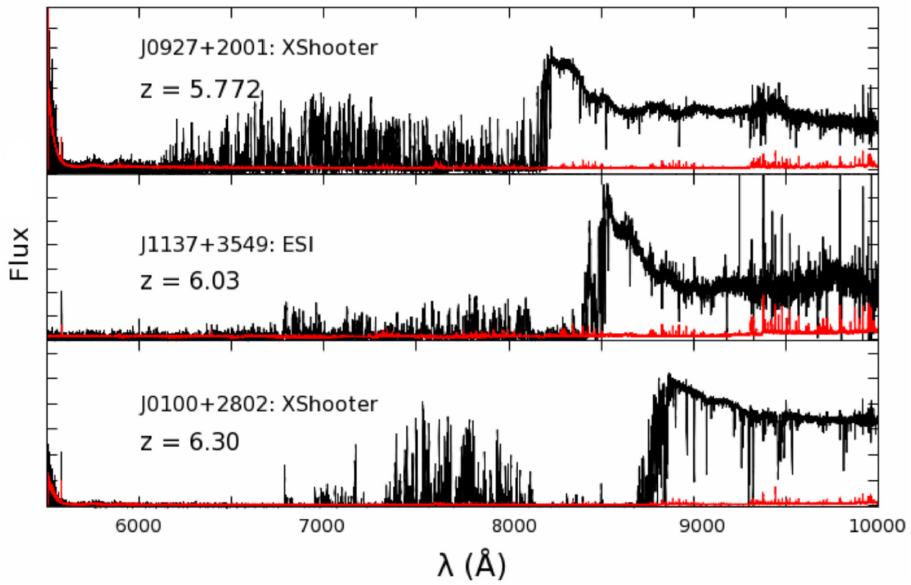

Figure 1. New quasar spectra used in this work. Details of the observations can be found in Table 3.

in e.g. Becker et al. (2015b). The spectrum was extracted optimally (Horne 1986) using 10 km s^{-1} bins after being flat-fielded and sky-subtracted following Kelson (2003). Custom telluric absorption routines were used as presented in Becker et al. (2012).

We obtained a 3000s ESI spectrum of the z= 6.01 quasar SDSS J1137+3549 on the 2016 March 18.

A deep X-Shooter spectrum of J0100+2302 was obtained in collaboration with Max Pettini over 2015 and 2016 as part of the 13 h program 096.A-0095(A). Here, we make use of only one exposure of 1800 s of the object, which is nevertheless a great improvement upon the previous LBT-MODS spectrum of the quasar.

2.7 Sample properties and notes on individual objects

Our 62 quasars have source redshifts in the range $5.70 < z < 7.08$ with a peak at $z \sim 6.0$ and a distribution as shown in Fig. 2. We investigate the Lyman-α forest over $1041 < \lambda_{\rm rest} < \sim 1178$ Å, resulting in a redshift coverage shown in Fig. 3 with up to 59 lines of sight covering the interval $5.4 < z < 5.5$. These distributions vary slightly depending on the choice of proximity-zone cut-off.

Redshifts for the objects in our sample are based the on best available estimates using nebular lines (such as [CII]) whenever possible. See Jiang et al. (2016) for the origin of the measured redshifts of SDSS quasars. Since we are primarily concerned with measuring Lyman-α opacity in the IGM, accurate values for the quasar redshifts are only relevant to the exclusion of quasar proximity zones from the analysis. In this work, we are not attempting to measure the evolution of quasar proximity zone length across redshift. We use a fix cut-off for the end of the proximity zone of $\lambda_{\rm end,\ prox} = 1178$ Å after checking that this is a reasonable choice and that more strin-

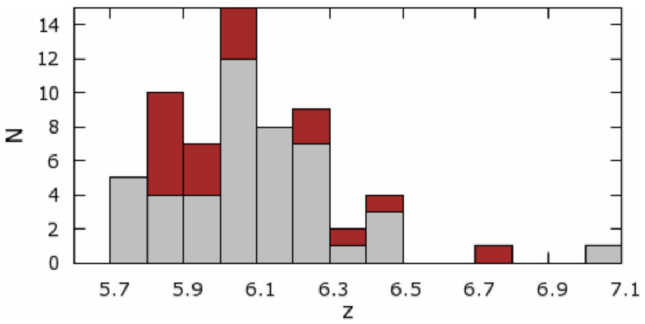

Figure 2. Redshift distribution of the quasars included in our sample. Red indicates the whole sample, while grey corresponds to the 'SILVER' sub-sample of objects with S/N > 5.

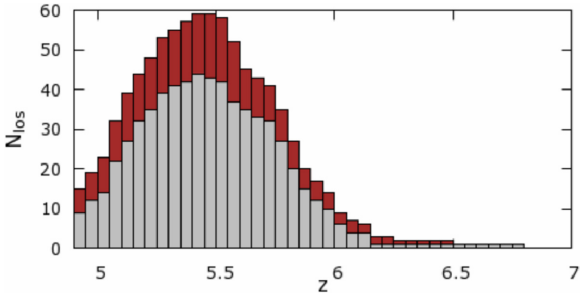

Figure 3. Cumulative number of lines of sight covering a particular redshift. Red indicates the whole sample, while grey corresponds to the 'SILVER' sub-sample of objects with S/N > 5.

gent criteria do not affect the results. This analysis is presented in Section 3.1.

We list the S/N for our spectra in the fourth column of Table 1. The S/N measurement is complicated by the disparate resolutions and redshifts of the quasar spectra, and because common sky lines fall at different rest wavelengths across the sample. To measure S/N, we first normalize the spectrum by a power law (PL) as described below, then keep the pixels located at $1275 < \lambda < 1285$ Å which are not affected by sky lines. This wavelength range covers a portion of quasar spectra minimally affected by broad emission lines. We present here the mean S/N per 60 km s^{-1}. The S/N is then computed as,

$$\mathrm{S/N} = \left\langle \frac{F}{\epsilon} \right\rangle \cdot \sqrt{N_{60}} \quad (1)$$

where ϵ is the error and N_{60} the number of pixels per 60 km s^{-1} interval. This is computed using $N_{60} = 60.0/\Delta v$, where Δv is the pixel size in km s^{-1}. For spectra where bins of fixed wavelength interval, $\Delta\lambda$, are used, rather than a fixed velocity interval, Δv is measured at $\lambda = 8000$ Å. While this is not the only way of homogeneously measuring spectral S/N, it is sufficient for our purposes to discriminate between data quality regardless of resolution, and has the advantage of being invariant under rebinning of the spectra. The values obtained range from S/N = 1.8 for J2325−5229, a DES–VHS quasar with continuum emission barely above the detection threshold, to S/N = 96.8 in a deep X-Shooter exposure of J1319+0959 first used in Becker et al. (2015b).

Out of the quasars in our sample, none show the characteristic features of broad absorption line (BAL) spectra or contamination by a damped Lyman-α system (DLA). Such objects were explicitly excluded during the sample assembly, with BAL and DLA features accounting for 5 out of 30 object rejections. We note that the fraction of quasar spectra displaying these features (5 out of 92 or about 5 per cent) is lower than measured at later times. This could be due to the selection techniques employed to discover high-redshift quasars, as the presence of a BAL feature diminishes the photometric colours most commonly used to select quasar candidates as dropouts. It is also likely that some contamination by DLAs has gone undetected in our sample. Due to the saturation of the Lyman-α forest, the most reliable way to detect and remove DLAs from the sample would be by detecting associated metal absorption at the DLA redshift. Mg II is unfortunately not visible for the redshifts of interest here, and the quality of the spectra is insufficient to detect typical C IV absorption systems in the majority of cases. Only deep X-Shooter spectra would provide sufficient coverage and sufficient S/N to completely remove DLA contamination at $z > 5.5$.

3 METHODS

quasarquasarThe spectra are first normalized by fitting a PL to the unabsorbed continuum. The portion being fitted extends from 1270 to 1450 Å in the rest frame of the quasar; the range 1270–1350 Å is used instead when the spectral coverage stops short of 1500 Å to avoid portions of the spectrum affected by the falling response of the instrument. This is the case for instance for spectra of $z > 5.7$ quasars taken with the MMT or MagE, whose coverage extends to $\lambda = 10\,000$ Å, but the response of which decays significantly from $\lambda \gtrsim 9700$ Å. Pixels affected by sky lines are excluded and a first PL fit is made, from which we then exclude any pixels for which $|F - F_{\mathrm{PL}}| > 2\epsilon$. The remaining flux is then fit with a PL again, and the process repeated a second time with a deviation coefficient of 1.5 to ensure convergence. Finally, the full flux array is divided pixel-by-pixel by the best-fitting PL function thus obtained.

Three objects which displayed too little continuum (due to a combination of high redshift and spectrograph wavelength coverage) are excluded from the analysis, since no satisfactory estimate of the continuum could be obtained. The continua for all other objects were checked visually. We checked that the best-fitting PL parameters were robust to small changes in the fitting window bounds. The effects of window choices were run all the way through the analysis; we find an end effect on values of τ of magnitude $\Delta\tau \lesssim 10$ per cent. This effect will be detailed in Section 4.3, where the only differences between our measurements and those of Becker et al. (2015b) are due to small differences in the choices of continuum fitting. These errors are in all cases much smaller than the effect of cosmic variance.

We measure the average transmitted flux in windows of 50 comoving cMpc h^{-1} extending from the end of the quasar's proximity zone at $\lambda_{\mathrm{rest}} = 1178$ Å down to the onset of Lyman-β absorption (1041 Å in the rest frame). The average continuum-normalized flux is transformed into effective opacity following $\tau_{\mathrm{eff}} = -\log(\langle F \rangle)$ and associated to the redshift corresponding to the middle of that 50 cMpc h^{-1} region. The analysis is repeated for window sizes of 10, 30, and 70 cMpc h^{-1}.

We treat non-detections of transmitted flux in two different ways. First, following previous work, we take the upper limit on the flux to correspond to twice the error in the flux over the measurement window. If individual peaks of transmission are detected at more than 2σ significance over that range, then we take the lower limit on the flux to be equal to twice the flux in those peaks alone following $F > F_{\mathrm{peaks}} - 2\sigma_{\mathrm{peaks}}$, where σ_{peaks} is the error over the wavelength covered by peaks (Becker et al. 2015b). This allows us to compare our results to the previous samples of Fan et al. (2006) and Becker et al. (2015b) which are a subset of our catalogue. The Lyman-α opacities in these two samples were not measured in identical ways, as the lengths of the excluded proximity zones and the details of the continuum fitting were subtly different. This might have resulted in a mild tension between the two samples, which we can now harmonize by

(i) doing a bootstrap re-sampling of our catalogue to mimic previously used sample sizes, and
(ii) treating both samples identically through the same continuum fitting routine and same proximity zone exclusion technique.

Secondly, we treat upper limits by plotting the most optimistic and pessimistic bounds on the cumulative distribution function (CDF). The optimistic bound is given, as above, by taking the intrinsic average flux to be equal to two times the average error over the measurement window, i.e. just below detection sensitivity. However, different spectrographs with different exposure times will be sensitive to different thresholds: for instance, none of the data in our sample could measure an effective optical depth $\tau_{\mathrm{eff}} \geqslant 8.0$. To reflect this ambiguity, we attribute maximal opaqueness ($\tau_{\mathrm{eff}} \rightarrow \infty$) to all non-detections in order to obtain a 'maximally pessimistic bound' (so-called due to the increased difficulty of reconciling this outcome with current reionization models). The 'true' CDF will necessarily lie in-between these two extremes as long as the bounds are resolved.

3.1 Proximity zone exclusion

We aim to measure the Lyman-α opacity of the IGM. In order to achieve this, we need to avoid any bias introduced by the quasar

proximity zones: the regions immediately surrounding the quasars where the ionization of the gas is enhanced due to ionizing radiation from the object themselves. In the past, cut-offs for quasar proximity zones were chosen either on a case-by-case basis as the point where the quasar's Lyman-α flux had fallen below 10 per cent of its peak value (Fan et al. 2006; Eilers et al. 2017) or chosen as a fixed value of 1176 Å determined based on a small sample of objects (Becker et al. 2015b). The former definition is not useful in the context of a sample containing spectroscopic data of varied resolution, since clumps of neutral gas within the proximity zone might be resolved by some instruments but not others. A fixed-value cut-off is therefore more suited to a large data set and facilitates future refinements of the measurements.

To ensure that the traditional value of 1176 Å is sufficiently stringent as to remove all proximity zone influence, we first plot a stacked spectrum of our entire catalogue in the range $1100 < \lambda < 1215$ Å (Fig. 4). The stacking was carried out by interpolating the spectra onto a common wavelength array after normalizing them by a fitted PL and removing bad pixels. For the purposes of the stacking, objects with different measurements errors are not weighed differently. Some interesting features are visible, such as the slight increase in average opacity along lines of sight with redshift and the average PL shape of the proximity zone. Based on the stack, we see that the proximity zone influences average transmitted flux at $\lambda > 1190$ Å, but effects further away are unclear. To confirm and refine this, we incrementally increase the amount of excluded flux blueward of the Lyman-α line and compare the resulting CDFs. This is equivalent to restricting the measurement to spectrum segments which are increasingly distant from the redshift of interest. The results are shown in Fig. 5 for several redshift bins. The effect of the proximity zone flux is visible as a modest decrease in opacity when a cut-off of $\lambda = 1190$ Å is used. A two-sample KS test (Kolmogorov 1933) yields levels of agreement $p > 0.8$ between the $\lambda = 1180$ and 1170 Å cases, indicating that the shape of the CDF has converged. Mild disagreement is obtained with the $\lambda = 1190$ Å case at $z = 5.8$ and 6.0 ($p > 0.50$ and 0.20, respectively). We therefore adopt a value of the proximity zone end at $\lambda = 1176$ Å in the rest of the paper.

Individual quasars showing anomalously long proximity zones (whether due to extreme bolometric luminosities, location in an underdense IGM region, or chance) could be present in the sample and would not appear in the stacks in Fig. 4. The resulting contamination could potentially bias the average opacities to be too low. However, we do not find any such objects in the sample by visual inspection. Uncovering trends in quasar proximity zones is beyond the scope of this work, and it is enough for our purposes to confirm that no boost to average flux is seen at $\lambda < 1176$ Å.

4 RESULTS

4.1 Comparison to previous studies

As a first test of our procedure, we reproduce the CDF presented in Becker et al. (2015b) using the spectra of 24 out of 27 $z > 5.7$ quasars used in that work, which are a subset of our catalogue. Fig. 6 presents the results at $5.5 < z < 5.7$ and $5.7 < z < 5.9$. The latter measurement makes exclusive use of those 26 quasars, and therefore any deviations are due entirely to subtle differences in the continuum fitting – such as the precise wavelength ranges used and the number of sigma-clipping iterations. In addition, the opacities of the spectra used in Fan et al. (2006) were not recomputed in Becker et al. (2015b), giving rise to a separate set of slight discrepancies. All of our measurements of $\tau_{\rm eff}$ in 50 cMpc h^{-1} windows agree within error with those quoted in the original papers. The Becker et al. (2015b) results at $5.5 < z < 5.7$ make use of four quasars at $z < 5.7$ which are not used in our sample. Nevertheless, the shapes of the cumulative PDFs are in excellent agreement, and the measurements of $\tau_{\rm eff}$ in individual windows all agree within error.

Next, we compare our results with those Becker et al. (2015b) by computing the CDF obtained from a random sub-sample of the size used by those authors from our larger sample. The contours of one hundred such realizations are plotted in Fig. 7. At all redshifts, we find the results are in statistical agreement, with a mild tension ($p < 0.5$) at $5.7 < z < 5.9$ where our work finds a slightly lower average opacity.

4.2 New Lyman-α distributions

Fig. 7 present our results compared to the previous CDFs of Becker et al. (2015b). As done in Becker et al. (2015b), the CDFs in Fig. 7 include lower limits. Fig. 8 presents the same results, plotted to show the 'pessimistic' and 'optimistic' bounds described earlier. The results over $4.9 < z < 5.7$ are completely consistent with previous studies. We find a clear, well-defined tail of high-opacity ($\tau_{\rm eff} > 3$) lines of sight at redshift $z \sim 5.2$. This trend was already visible in the CDF reported in Becker et al. (2015b). Roughly, ∼20 per cent of lines of sight at $z = 5.2$ have opacities $\tau_{\rm eff} > 2.5$, which might pose problems for IGM models that assume a spatially uniform UVB and temperature–density relation.

At $z \sim 5.6$, we find a small but significant tail of transparent lines of sight, with roughly ∼20 per cent of measurements showing $\tau_{\rm eff} < 2.5$. This tail was not visible in the Becker et al. (2015b) sample as most of the relevant objects were not included. The two samples are consistent according to a two-sample KS test at all redshifts ($p > 0.80$). At $z \sim 5.8$, we find that opacities are slightly smaller than the ones previously reported. Our sample for $z \sim 5.8$ is of comparable size to Becker et al.'s (2015b) samples at $z \sim 5.2$ and 5.4, so that small differences are expected between our measurement and a 'true' representation of cosmic variance in the same way as seen at lower redshifts.

At $z \sim 6.0$, our sample is smaller than all the ones used in Becker et al. (2015b) at lower redshift and the results should be interpreted with caution. Seven out of eleven 50 cMpc regions included in our SILVER sample display residual peaks of transmission, while the remaining four pose tight constraint on transmission. We find a very high average opacity of $\tau_{\rm eff} \sim 4.5$. Such opacities are only accessible to current spectrographs with large time investments. We will examine this effect in more detail in the next Section by dividing our sample based on data quality.

In Fig. 9, we plot the distribution function of Lyman-α opacity across redshift. We distinguish between detections and lower limits using separate histogram colours. The distributions are clearly non-Gaussian, with peak values increasing linearly with redshift. The tail of opaque lines of sight at $z \sim 5.2$ is clearly visible and appears smooth and well sampled.

The effect of varying the size of the integration window is shown in Fig. 10. Although the effect is subtle, decreasing the window size tends to broaden the distribution, as expected. This is a natural consequence of cosmic variance. The broadening is particularly pronounced when the window size is decreased below 30 cMpc h^{-1}. The redshift range $5.1 < z < 5.7$ is more clearly affected, possibly because these redshifts are better sampled. We find no statistically significant difference between bins of 30, 50, and 70 cMpc h^{-1} at any redshift ($p > 0.8$). The distributions with binning sizes of 10 cMpc h^{-1} are strongly discrepant, with a two-sample

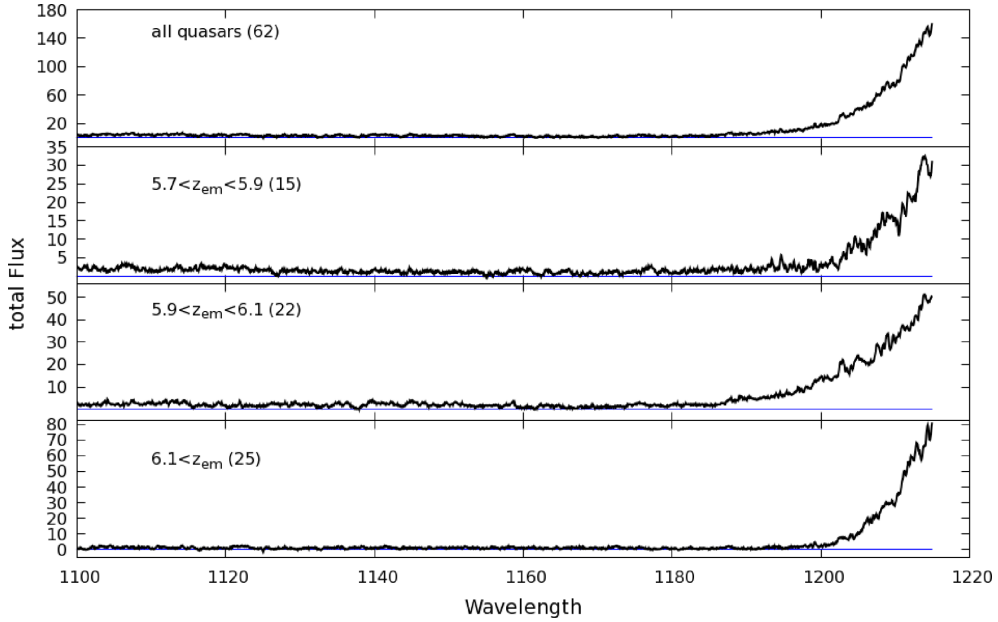

Figure 4. Stack of flux over $\lambda = 1100$–1215 Å of 62 $z > 5.7$ quasars. Spectra were normalized and sky lines masked before stacking. While the proximity zone transmission has fallen considerably by 1180 Å, the exact end of the host quasar's influence on the flux is unclear. Five spectra are excluded as described in Section 2.7. Panels show the evolution of the stacked spectrum over $5.7 < z < 5.9$, $5.9 < z < 6.1$, and $6.1 < z$. The thin blue lines show a total flux of zero.

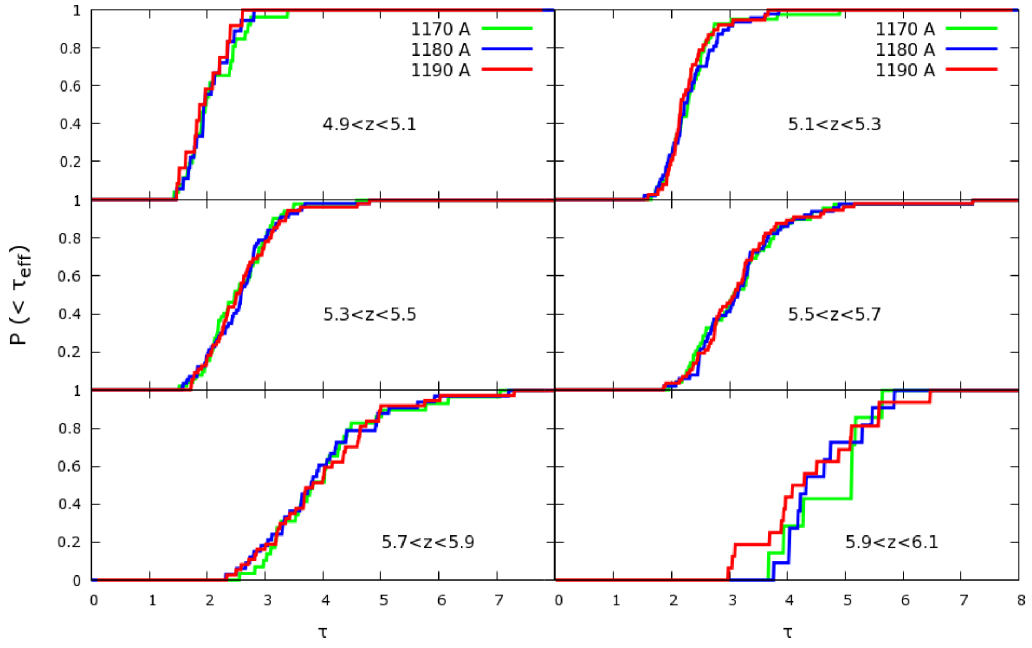

Figure 5. Effect of incrementally increasing the excluded proximity zone size on the Lyman-α CDF at various redshifts (see also Fig 4). By ending the proximity zone at $\lambda = 1190$ Å, the average opacity is affected at $z < 5.3$ and $5.5 < z < 5.7$. However, no statistically significant difference is seen between a cut-off at $\lambda = 1180$ Å and the very conservative case $\lambda = 1170$ Å, at any redshift. Throughout this paper, we adopt the traditional cut-off $\lambda = 1178$ Å.

KS test finding a probability $p < 0.01$ that they were drawn from the same sample as the distributions with larger binning windows.

4.3 Effect of data quality

We select sub-samples from the quasar catalogue based on the S/Ns. A 'GOLD' sample is chosen with S/N $\geqslant 11$ to match the S/N of the worst spectrum used in McGreer et al. (2015). This yields a sample of 33 high-quality spectra, nearly halving the sample. Similarly, we construct a 'SILVER' sample by applying a less stringent cut of S/N $\geqslant 5$, matching the data quality from Eilers et al. (2017). This yields 45 lines of sight. For consistency, we will refer to the full sample as the 'BRONZE' sample. We note that the sample of 26 quasars used by Becker et al. (2015b), the largest one so far, includes measurements from Fan et al. (2006) made from spectra with S/N much lower than these thresholds – down to S/N = 3.2. The results are shown in Fig. 11. There is no significant trend with data quality at $z < 5.7$, where the distribution is well sampled even by the small

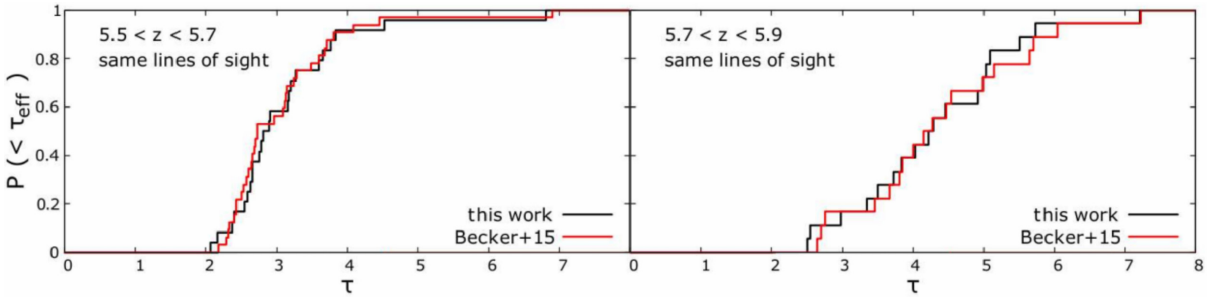

Figure 6. Reproduction of the Becker et al. (2015b) opacity PDFs at $5.5 < z < 5.7$ (left) and $5.7 < z < 5.9$ (right). The same lines of sight are used, except for four quasars at $z < 5.7$ that are excluded from our work for the lower redshift case. Differences are accounted for by slight differences in the continuum fitting between the authors and previous measurements taken from Fan et al. (2006).

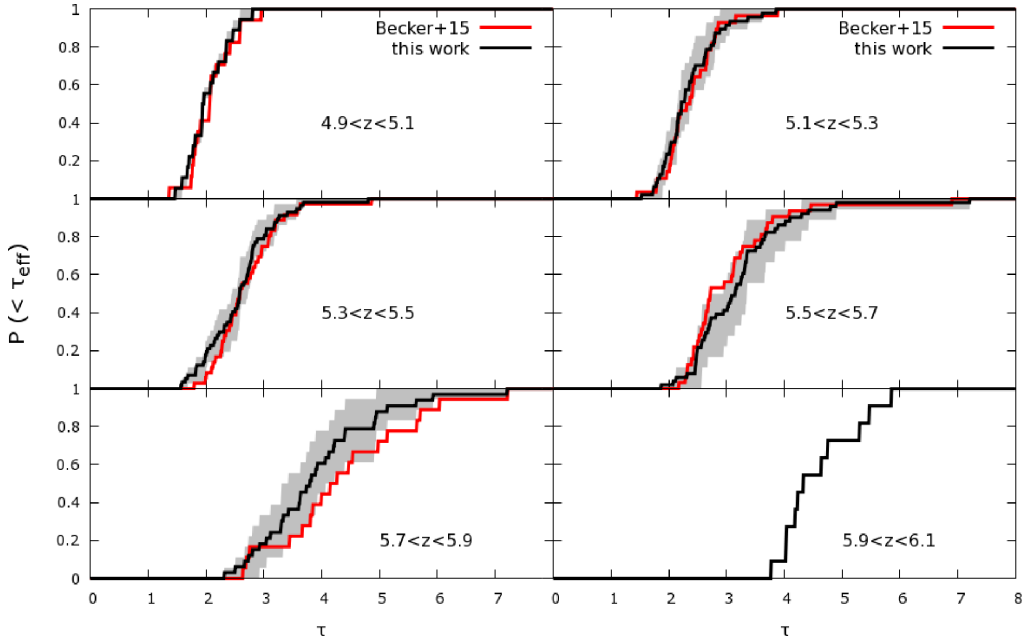

Figure 7. New results, obtained using the method described in Becker et al. (2015b). Only spectra of moderate or good quality (S/N > 5.0, 'SILVER' sample) are used, and non-detections of transmitted flux are treated as data points with values of twice the average error (see the text). No significant discrepancy with previous results is found.

GOLD sample (two-sample KS test $p > 0.8$). A disparity appears at $z > 5.7$.

The differences between the SILVER and GOLD samples at $5.7 < z < 5.9$ are due to the small sample size of the GOLD sample. The difference in number of lines of sight in this range is a factor of 2.5, which reflects the fact that very high-quality spectra are harder to obtain for quasars at $z > 6.0$. The SILVER and GOLD sample are marginally consistent according to a KS test ($p < 0.2$).

On the other hand, the sizes of the SILVER and GOLD samples are similar at $5.9 < z < 6.1$, and agree with each other well. However, the additional lines of sight included in the BRONZE sample are of insufficient quality to distinguish opacity beyond $\tau_{\rm eff} \gtrsim 3$. Since the mean opacity measured in the SILVER sample is roughly $\tau_{\rm eff} \sim 4.5$, these S/N < 5 spectra yield upper limits (equal to twice the error) which are very poor in comparison. The small sample size in this bin (8 measurements in the GOLD sample, and 16 in the BRONZE one) mitigates the significance of this discrepancy, with the KS level indicating only mild discrepancy ($p < 0.2$). In addition, two of the BRONZE lines of sight do show tentative signs of residual transmission. The $z = 6.34$ quasar J1148+0702 displays a transmission peak within 6 Å of the formal end of the proximity zone, while the $z = 6.23$ quasar J2325 displays such a peak outside of its proximity zone but has an S/N of 1.8, making it impossible to definitely rule of reduction issues. Further scrutiny of these objects is required in order to determine whether these peaks may be related to particularly long and sporadic proximity zones.

In light of these results, we decide to adopt the SILVER distribution in every instance in this paper where the data are presented or analysed in the form of a CDF. The maximum-likelihood method described above has been explicitly designed to account for observational errors and sensitivity, and we accordingly use the BRONZE sample only in Section 6.

5 COMPARISON WITH MODELS

In this section, we compare the updated CDFs of Lyman-α transmission in 50 cMpc h^{-1} windows with three simulations. Here, we briefly describe these simulations and outline their most relevant features.

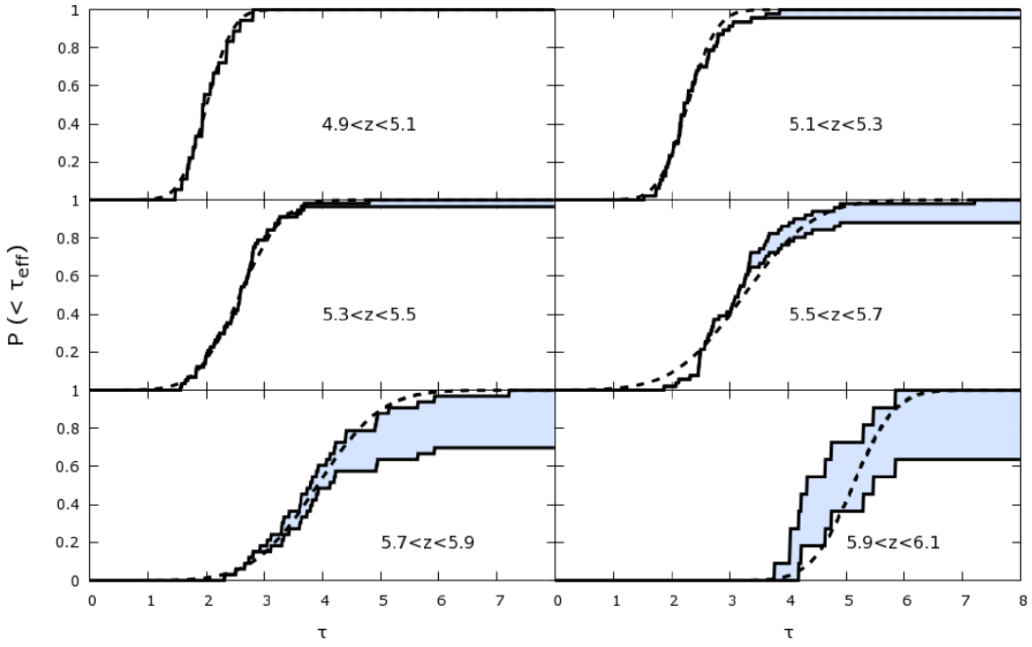

Figure 8. New results, plotting the most optimistic and most pessimistic contours based on the intrinsic values of non-detections. The leftmost contour corresponds to non-detections have intrinsic values of twice the average error (as in Fig. 7), while the rightmost contour assumes non-detections are maximally opaque (see the text). The thin dashed line displays the most likely lognormal distribution computed in a maximum-likelihood scheme (see Section 6).

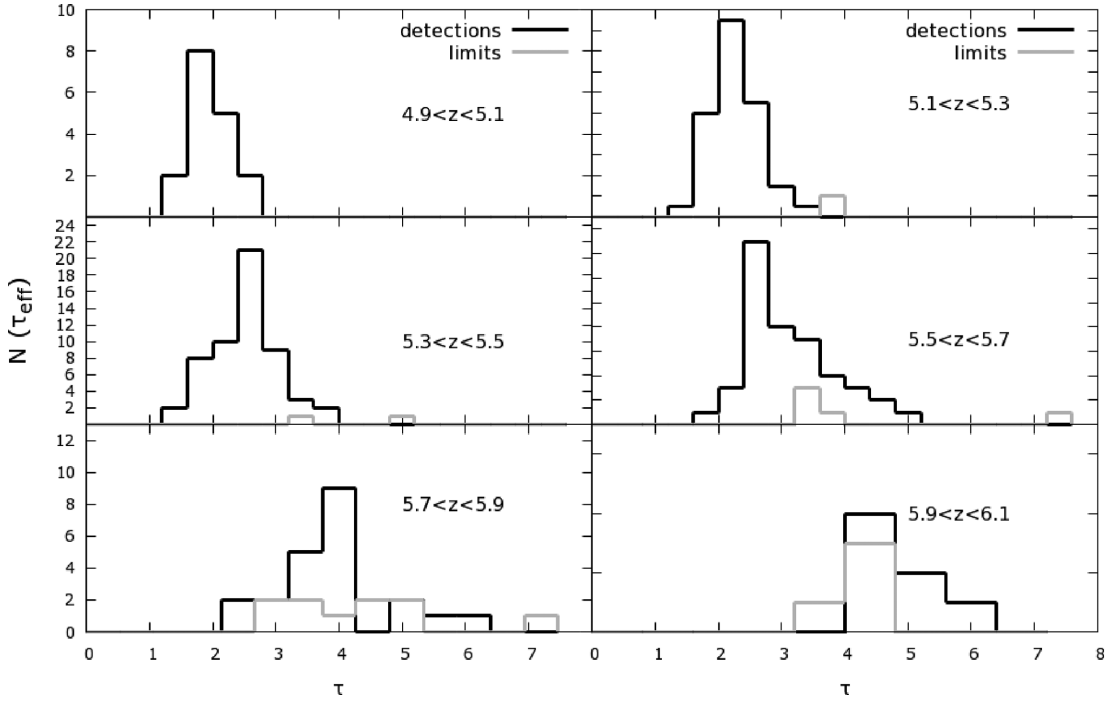

Figure 9. Differential distributions of opacity in 50 cMpc h^{-1} bins, showing detections in black and lower limits in grey.

When comparing predictions from these numerical simulations to observational results, it is important to keep in mind a few caveats. First, all of the following numerical models explicitly rescale the ionizing background intensities to match the observed mean effective optical depth of the observations presented in this paper, $\langle F \rangle_{\rm obs}$, by freely choosing a parameter A such that:

$$\langle e^{-A\tau_i} \rangle = \langle F \rangle_{\rm obs}. \quad (2)$$

At low redshift ($z \lesssim 5.7$), this rescaling is small and is somewhat justified by the difficulty of self-consistently generating the ionizing UVB. In the following analysis, all simulation snapshots have been rescaled in this way to observed $\langle F \rangle_{\rm obs}$ for each redshift bin. The values of $\langle F \rangle_{\rm obs}$ are computed using the SILVER sample of objects with S/N > 5, and are shown in Table 4.

These simulations all use the UVB prescription of Haardt & Madau (2012, HM12) as a starting point, which incorporates the

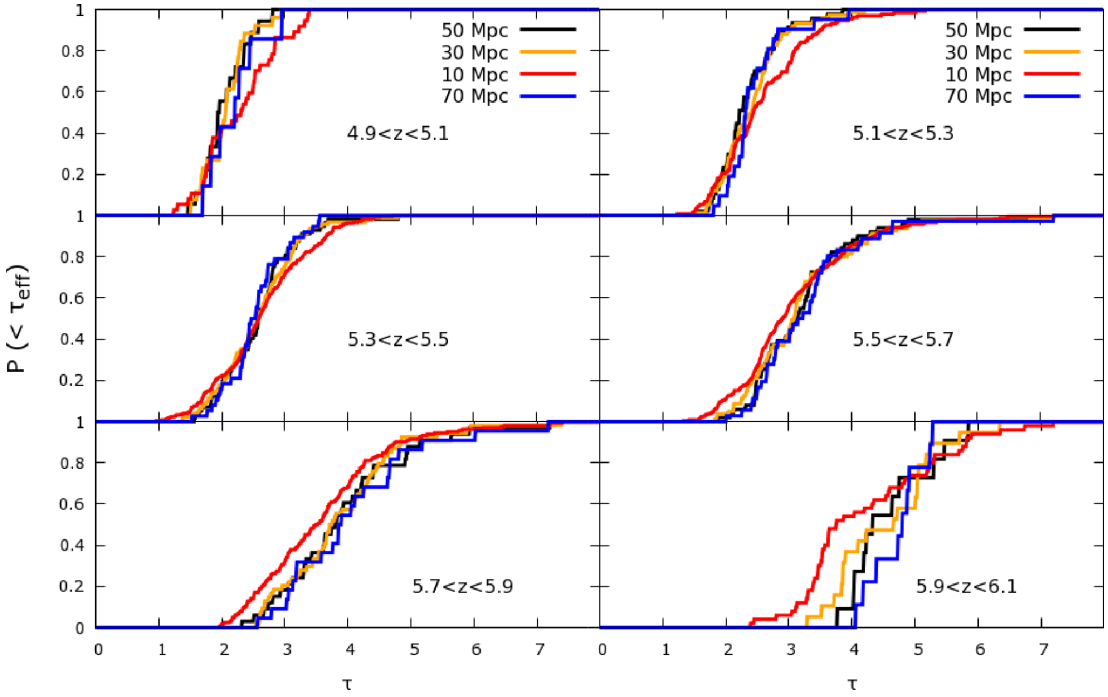

Figure 10. The effect of varying the size of the window over which Lyman-α transmission is measured. No significant effect is seen between windows of 30, 50, and 70 cMpc h^{-1} at any redshift, suggesting that fluctuations occur on even larger scales. Binning the data in 10 cMpc h^{-1} windows strongly affects the distribution, in particular at lower redshifts where it results a broader distribution.

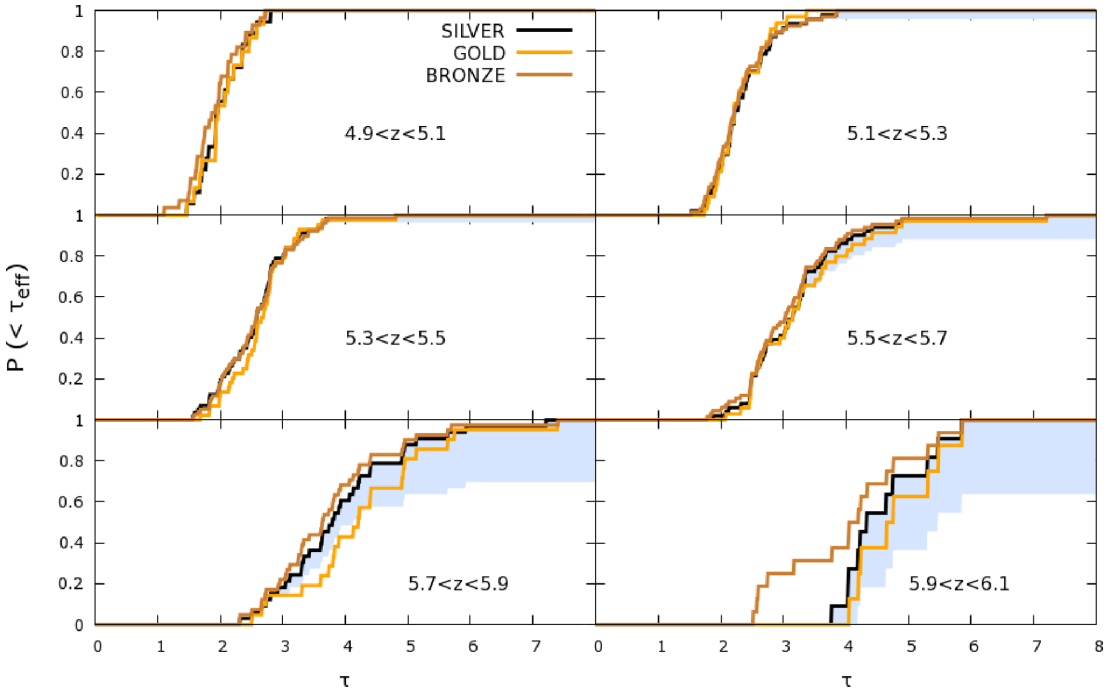

Figure 11. CDFs of Lyman-α opacity across redshift, computed using the full sample (black), the SILVER sub-sample of 51 objects matching the quality of data used in Eilers et al. (2017) (S/N $\geqslant$ 5.3), and the GOLD sample of 35 objects which match the quality from McGreer et al. (2015) (S/N $\geqslant$ 11.2). Shaded blue areas show the 'optimistic' and 'pessimistic' bounds presented in Fig. 8. At $z < 5.5$, the distributions are well resolved by all samples and the distributions therefore agree. At $5.5 < z < 5.9$, the GOLD distribution lies between the bounds shown in Fig. 8. At $z > 5.9$, the difference is attributable to the small sample size of the sub-samples (see the text).

Table 4. Emissivity rescaling factors (α) used to tune the simulations discussed here. The factors are chosen to match the observed flux F following $\langle F\rangle_{\rm obs} = \langle \exp(-\alpha \cdot \tau_{\rm los})\rangle$ (see the text). The first column gives the measured values of $\langle F\rangle_{\rm obs}$. To obtain the most accurate measurement possible, only the GOLD sample was used. The errors are estimated using bootstrap re-sampling.

z	$\langle F\rangle_{\rm obs}$	Chardin Puchwein & Haehnelt (2017)	Keating et al. (2017)	Sherwood
5.0	0.135 ± 0.012	N/A	1.703	0.662
5.2	0.114 ± 0.006	N/A	1.522	0.590
5.4	0.084 ± 0.005	0.878	1.509	0.565
5.6	0.050 ± 0.005	0.848	1.135	0.590
5.8	0.023 ± 0.004	0.841	1.055	0.666
6.0	0.0072 ± 0.0018	N/A	0.944	0.796

best available estimates of the nature of ionizing sources, the ratio of galaxy to quasar contributions, the escape fraction, the spectral shape of sources, and other factors. The precise values of these parameters are not known, and vary across redshift. The HM12 emissivity is therefore used as a best guess, and the final rescaling of the emissivity reflects the known inaccuracy in the model. The rescaling is therefore not only simulation- and redshift-dependent, but also resolution-dependent, since the small-scale recombination and self-shielding effects necessary to calculate the UVB self-consistently are currently beyond the reach of numerical simulations. In Table 4, we list the values used to rescale in optical depths in each case (α), chosen to match the observed flux F following $F = \langle \exp(-\alpha \cdot \tau_{\rm los})\rangle$. At high redshift ($z \gtrsim 5.9$), this rescaling procedure becomes less valid because the correction is not small. For instance, the mean flux values of the Sherwood simulation used here had to be rescaled by a factor >10 at $z = 6$. This reflects the fact that the HM12 background is a bad representation of the ionizing emissivity at high redshift, and ideally should not be used.

Secondly, the timing of reionization is a free parameter in most of the following models. The Sherwood simulations, and the HM12 ionizing background, were designed to fit Lyman-α transmission at lower redshifts than explored here. Because the time evolution of Lyman-α transmission is slower at $z < 4.9$, the successful predictions of these cosmological simulations are usually robust to shifts up to $\Delta z_{\rm Re} \sim 0.2$ over the redshift range considered here (see e.g. Chardin et al. 2018).

5.1 Full forward modelling

To meaningfully confront simulated Lyman-α lines of sight with observations, it is important to post-process them in a way which mimics data. We take a full forward modelling approach when comparing the data to simulations, transforming simulated lines of sight into realistic observations before treating them in the same way as the data. This simplifies the comparison, and enables us to estimate the errors in an empirical way.

We implement this by selecting the same number of simulated lines of sight as present in the data at each redshift, and post-processing them with observational profiles. An observational profile consists of an instrumental resolution and an error array. Each selected simulated line of sight is randomly matched to such a profile drawn randomly from the observations relating to the redshift under study. The simulated spectrum is first mapped onto a corresponding wavelength array, convolved with a Gaussian with width of the instrumental resolution and rebinned onto the same wavelength array as the observation. Finally, noise is added randomly at each pixel following a Gaussian distribution with width corresponding to the observed error in that pixel.

The resulting post-processed lines of sight are equal in number to the observations for the corresponding redshift range, and the CDF extracted from both sets of lines of sight should now in principle be completely comparable. To get an estimate of the variance between random realizations, we run the entire process 100 times until the envelope of the CDF bounds converges. CDFs outside of those bounds – even by a single bin – therefore empirically have much less than one chance in 100 of being observed if the underlying transmission is given by the simulated model. These bounds are shown overlayed with the observational bounds in Figs 12 and 13 corresponding to the rare sources model, radiative transfer model, and uniform UVB cases, respectively. The raw predictions from the simulations, without post-processing, are all shown in Fig. 14.

5.2 The Sherwood simulation

The Sherwood simulation suite (Bolton et al. 2017) was designed to reproduce the Lyman-α forest over $2 < z < 5$ and test its sensitivity to a range of model parameters such as galactic and AGN-driven outflows, thermal histories, and cold/warm dark matter. With gas particle masses of $M_{\rm gas} = 9.97 \cdot 10^4 M_\odot$ and 2×2048^3 particles for a box size of 40 cMpc $\rm h^{-1}$, the Sherwood simulation used here possesses higher mass resolution than other larger scale cosmological simulations such as Illustris and the Evolution and Assembly of GaLaxies and their Environments simulation (EAGLE). The simulation is run using the hydrodynamics code P-GADGET3 (Springel 2005) and used ∼2680 000 core-hours of computing time. Bolton et al. (2017) compare simulated Lyman-α lines of sight with the results from Becker & Bolton (2013) and Becker et al. (2015b), finding remarkable agreement over $2.5 < z < 5$ with a slight lack of strongly opaque regions at $z = 2.0$. Because it was designed to match observations at redshifts less than $z = 5$, the Sherwood simulation uses a uniform UVB with a shape given by the HM12 model, in a scenario where reionization is driven mostly by galaxies and with no radiative transfer. The interrelations of hydrogen neutral fraction, temperature, photon mean-free path, and density are therefore not taken into account, and the simulations are expected to fail in the hydrogen reionization regime where the UVB is known to be inhomogeneous.

Here, we compare the 40 cMpc $\rm h^{-1}$ Sherwood simulation box with the Lyman-α CDF over $4.9 < z < 6.1$. Each measurement of $\tau_{\rm eff}$ requires stitching together two simulated lines of sight and truncating to 50 cMpc $\rm h^{-1}$; 2500 total values of $\tau_{\rm eff}$ are obtained. The model predictably falls short of reproducing the variety of line-of-sight opacities at $5.3 < z < 6.1$. A KS test shows the post-processed sets of predictions are excluded at $5.3 < z < 5.7$ ($p < 0.02$) and marginally disfavoured at $5.7 < z < 5.9$ ($p < 0.1$). It is perhaps more surprising that the uniform UVB model also

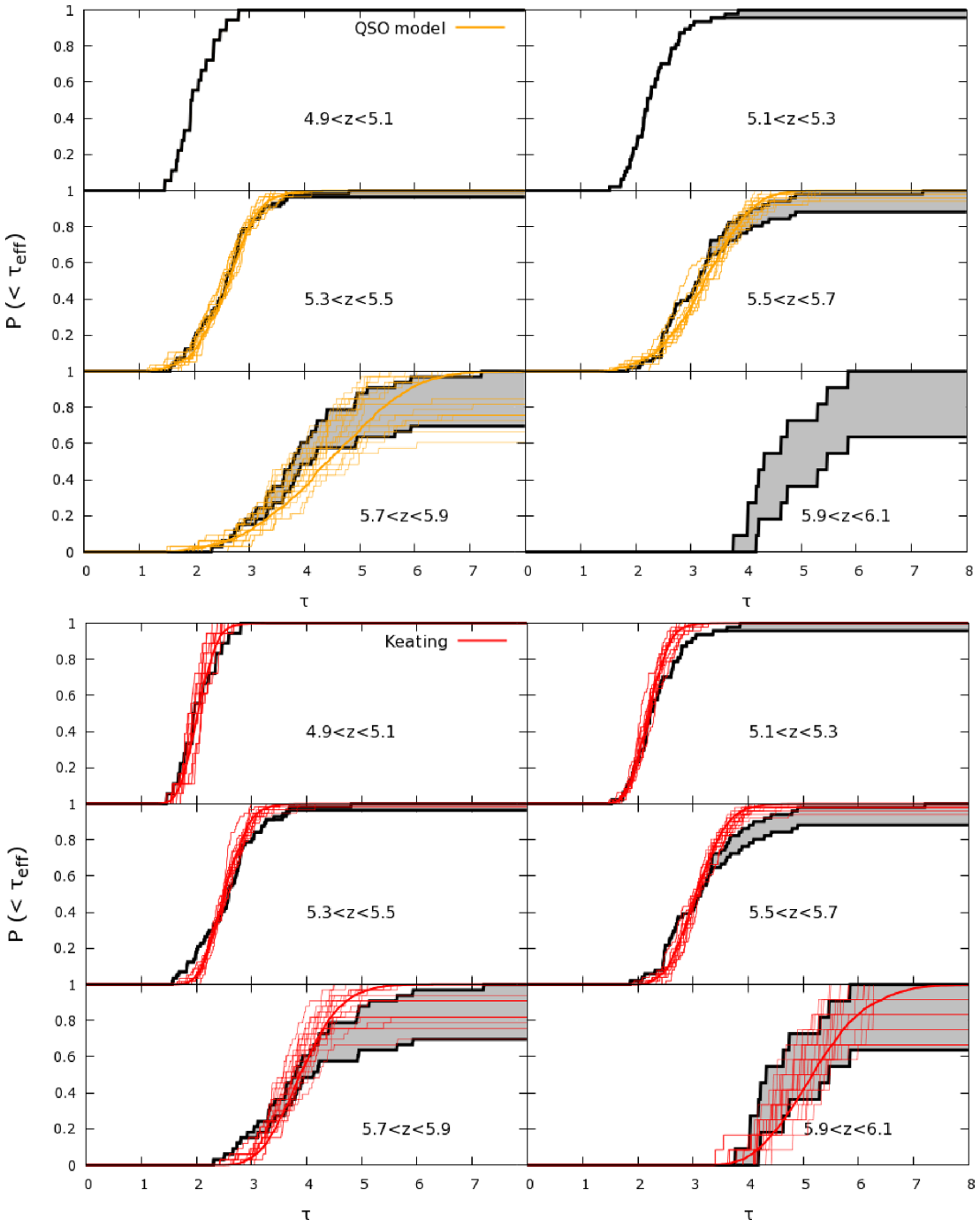

Figure 12. Comparison of the measured Lyman-α PDFs at $4.9 < z < 6.1$ with fully post-processed outputs of numerical simulations from Chardin et al. (2017) (top) and Keating et al. (2017) (bottom). The coloured contours show the envelope of the pessimistic and optimistic bounds for 100 realizations. Post-processing consists of randomly drawing a number of lines of sight from the simulations equal to the number of observations in the corresponding redshift range. The simulated lines of sight are then forward modelled to mimic the observed spectra (see the text).

fails at $5.1 < z < 5.3$ ($p < 0.03$), where line-of-sight variation is slightly more pronounced than previously reported. Another point of disagreement not reflected by statistical disagreement is that the simulations are never able to output lines of sight with $\tau_{\rm eff} > 3.5$ at $z \sim 5.2$ – such consistently opaque lines of sight simply do not exist inside the simulated boxes.

5.3 Radiative transfer simulation

In addition to the homogeneous-UVB Sherwood simulations, we compare our results to the full cosmological radiative transfer simulations of Keating et al. (2017). Following D'Aloisio et al. (2015), these simulations test the effect of regions ionizing at different redshifts on the spatial variations in the temperature–density relation. The temperature dependence of recombinations rates could then lead to increased fluctuations in Lyman-α opacity. Unlike previ-

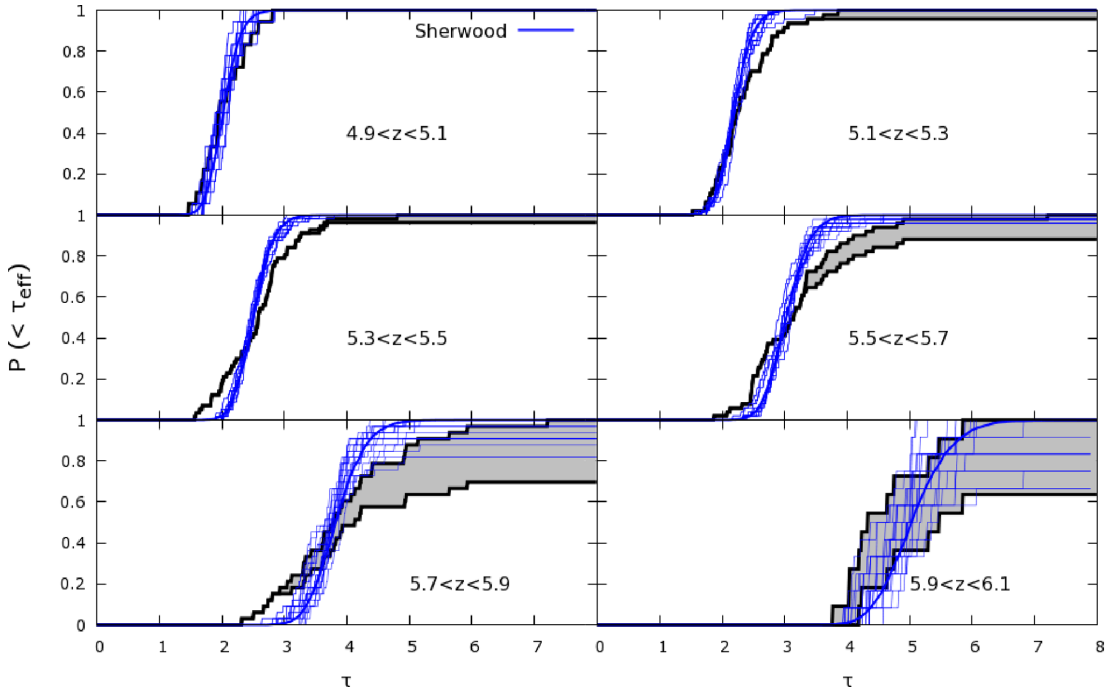

Figure 13. Same as Fig. 12 for lines of sight drawn from the Sherwood simulation (Bolton et al. 2017).

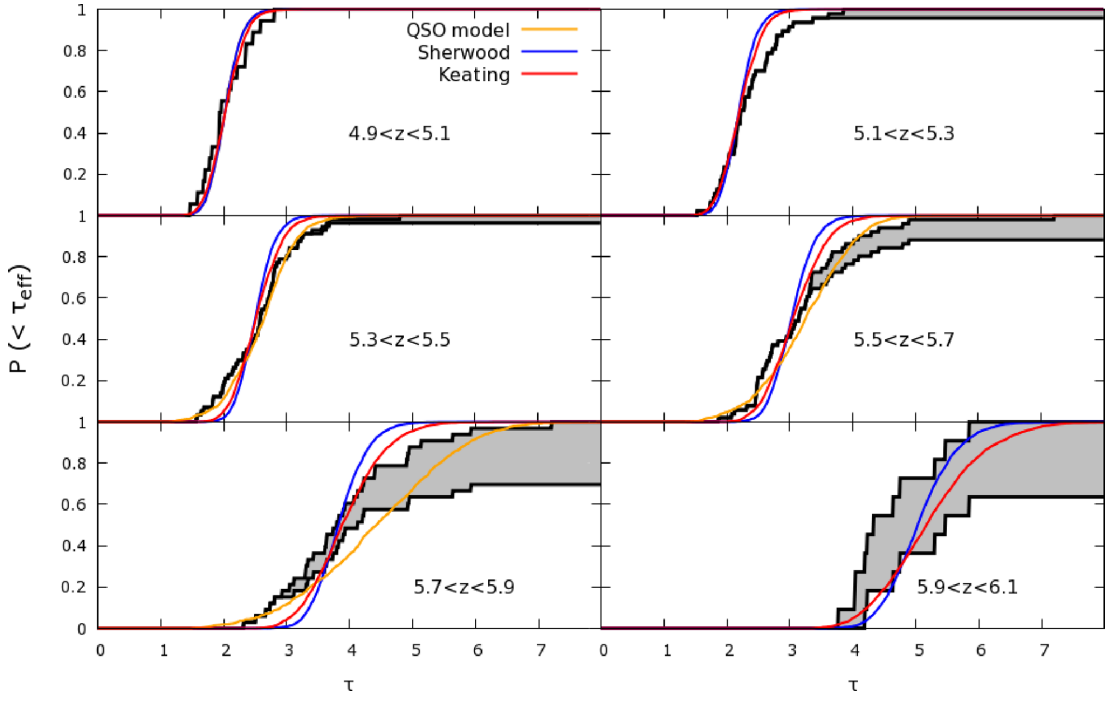

Figure 14. Comparison of the measured Lyman-α PDFs at $4.9 < z < 6.1$ with outputs from a range of numerical simulations. This plots shows only the solid lines from Figs 12 and 13, and the errors have been omitted for the sake of comparison.

ous models, Keating et al.'s simulations use an extended and self-consistent reionization history to boost the IGM temperature. The injected energy and history are chosen to match the temperature and photo-ionization rates of the IGM at $z \lesssim 5.0$ measured using the Lyman-α forest.

This difference to previous models turns out to be important, as Keating et al. (2017) find their more realistic choices of reionization heating do not reproduce the large Lyman-α opacity fluctuations previously reported. Choosing a higher ionization energy to match the IGM heating in D'Aloisio et al. (2015), they find the fluctuations are still not large enough, and moreover the produced lines of sight are in tension with low-redshift Lyman-α forest data as well as transmission peak statistics at high redshift.

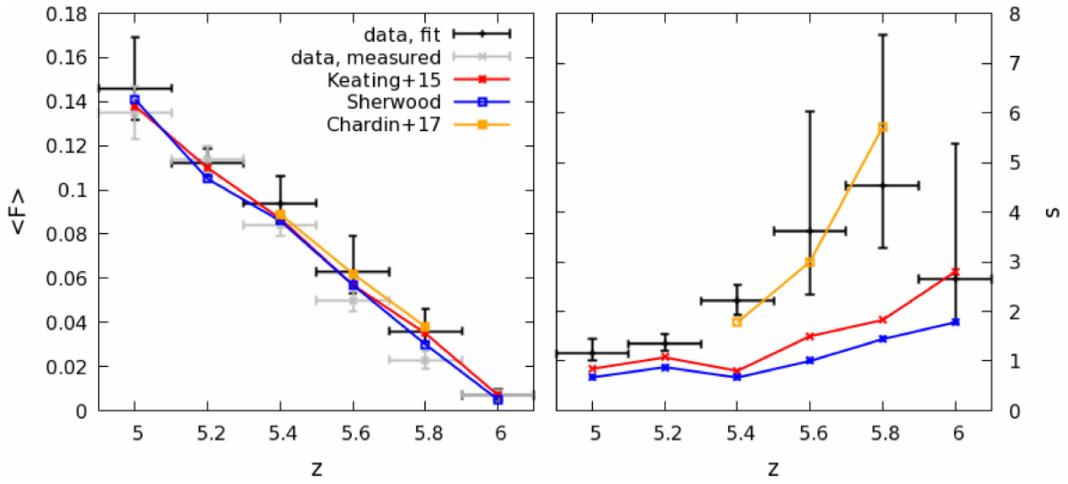

Figure 15. Evolution with redshift of the mean flux $\overline{F}$ (right) and the skewness parameter s (right) of Lyman-α transmission. A rapid decrease in mean flux with increasing redshift is accompanied by an increase in skewness, as the distribution of fluxes is increasingly non-Gaussian. Simulations are post-processed to match the mean flux measured from observations; the offset between observations and simulations at the highest redshift bins reflects the fact that the most likely intrinsic mean flux is lower than the measured mean flux.

The simulations are also run in P-GADGET3 but snapshots of the resulting density field are then post-processed to include the effects of temperature and ionization using monofrequency radiative transfer. Here, we use a 40 cMpc h^{-1} box with 512^3 mass particles, which should better capture large-scale variations of opacity than the higher resolution 20 cMpc h^{-1} box. Keating et al. (2017) compare their Lyman-α PDFs to data over $4.9 < z < 5.9$ and find no trend with box size. Here, we stitch together two simulated lines of sight for each of the 2500 total measurements of $\tau_{\rm eff}$. We find that this model, while performing better than the Sherwood simulation, does not provide a satisfactory fit to the Lyman-α CDFs. Statistical agreement between post-processed lines of sight and observations is improved at all redshifts with only the range $5.3 < z < 5.7$ being excluded ($p < 0.05$). Despite being marginally consistent at lower redshift ($p < 0.5$ at $5.1 < z < 5.3$), the model still does not contain any lines of sight with $\tau_{\rm eff} > 3.5$. Although including radiative transfer does increase line-of-sight variance, the effect is too small by at least factor of two. This is in agreement with the results of Keating et al. (2017).

5.4 Rare sources simulation

Finally, we compare the results to predictions of a quasar-driven reionization toy model from Chardin et al. (2017). These models include a density field produced by the hydrodynamics code RAMSES onto which radiative transfer is added in post-processing with the ATON code. They found the fluctuations in the UV produced by galaxies in the redshift range $5 < z < 6$ to be on scales too small (<50 cMpc) to account for the spread in Lyman-α opacity. A much better fit was found when rare, bright ionizing sources were added to the simulation with a carefully chosen spatial density. Such sources could be (faint) quasar , or alternatively extremely bright star-forming galaxies.

The simulation boxes of Chardin et al. (2017) are only 20 cMcp h^{-1} in size, but this is not a problem as the line-of-sight variance is mostly driven by the presence or absence of a strong ionizing source nearby. The simulations use 512^3 mass particles. Because of the smaller simulation volume, we have to stitch three simulated lines of sight together for each measurement of $\tau_{\rm eff}$. This results in 1020 measurements, a smaller number than in the previous cosmological simulations.

We find that the rare sources simulations marginally reproduce the CDF at $5.5 < z < 5.9$, and are the only model to do so out of the ones we tested ($p < 0.5$). We note however that the line-of-sight variance seems to disappear very quickly at lower redshifts, resulting in the model underestimating the opacity variance at $5.3 < z < 5.5$. Unfortunately, no snapshots were available at $5.1 < z < 5.3$, but it is unlikely that those would show a sufficient amount of opaque lines of sight, since those are already gone from the simulations at $z \sim 5.4$. However, we note that there might be room for reionization to occur later within this model, which could potentially ease the conflict. Chardin et al. (2017) also note that their simulations are in better agreement with the Lyman-α CDFs calculated with smaller window sizes of $l = 10$ cMpc h^{-1}. This is still the case with the updated measurements, as can readily be seen by comparing Figs 10 and 14.

There is also tension between this model and observations for low-opacity lines of sight at $z \sim 5.8$: in a quasar-driven scenario, low opacity regions arise purely due to proximity to a source quasar and are therefore not expected to disappear completely at high redshift, as long as the quasars are active. This appears to be in contrast with observations which do report that transparent lines of sight go missing at $z > 5.7$. However, this problem is mitigated by

(i) the smaller observed sample size at these redshifts, which means the discovery of even one transparent line of sight could ease the conflict, and

(ii) while the ionizing emissivity is already tuned to observations, it might be sensible to rescale the predicted opacity by a larger factor to improve the agreement with data (see later).

We note that the volume density of rare bright sources in this model was explicitly chosen to reproduce the Lyman-α CDFs of Becker et al. (2015b) which use 'optimistic' measurements i.e. following our leftmost CDF contour. It is conceivable that the model could be modified to reproduce a CDF closer to the mid-point of our contours. This will be discussed in more detail in the next section.

6 EMPIRICAL ANALYTIC FIT

The treatment of non-detections implemented above is conservative, but does not return a best fit or most likely distribution. Such a fit should ideally incorporate weighting of the observational constraints based on corresponding observational errors in a way where extra data, no matter how large the errors, should not make the fit worse. In order to achieve this, we perform a fully bayesian maximum-likelihood analysis. This requires a parametrization of the Lyman-α flux distribution; we empirically find that the data are well fitted by a scale-dependent lognormal distribution on the form,

$$P(F;\sigma,\mu) = \frac{e^{-\log(F/\mu)^2/2\sigma^2}}{F\sigma\sqrt{2\pi}}. \quad (3)$$

The lognormal parameters (σ, μ) can be recast into the more physically meaningful variables of *mean flux* $\overline{F}$ and *skewness parameter* s following

$$\overline{F} = \mu e^{\sigma^2/2}; \quad s = \left(e^{\sigma^2}+2\right)\sqrt{e^{\sigma^2}-1}. \quad (4)$$

This parametrization has the advantage of making the tuning used in simulations explicit: $\overline{F}$ in the simulations is chosen, at each redshift, to match the observations. The difference between data and models is then limited to the shape or skewness parameter s, on which meaningful constraints can be obtained. A small value of $s \lesssim 1$ indicates a roughly normal distribution, while $s \to \infty$ tends to a log distribution.

For each set of parameters (σ, μ), the likelihood L of the observations given those parameters is computed following

$$L_{\sigma,\mu} = \prod_{\text{obs}} \int_{F=0}^{1} P(F;\sigma,\mu) D_{\text{obs}} \quad (5)$$

where D_{obs} is the normalized probability distribution of a measurement. This is taken to be a Gaussian centred on the observed F and with variance equal to the error on F. D_{obs} represents the probability distribution of the intrinsic flux within a spectrum region and naturally weights the observations according to their observational errors. We implement the prior that the intrinsic flux is necessarily positive by defining D_{obs} only for $F \geqslant 0$. In this way, observations in which the mean flux is formally below the detection threshold, and even observations where the mean flux is formally negative, can be used as constraints on the underlying distribution of fluxes.

Following the likelihood ratio confidence bounds methods, the best-fitting parameters are found where the value of L is highest, with 68 per cent, 90 per cent and 95 per cent credibility regions found where $L/L_{\max} > 0.6099$, 0.2585, and 0.1465 respectively (Barlow 1989; see also Andrae 2010). This has the useful feature of being insensitive to multiplicative rescaling of D_{obs}. The post-processed predictions from simulations are obtained by forward modelling 100 simulated lines of sight which then go through the same pipeline as the observations.

The posterior distribution on $\overline{F}$ and s, and predictions from post-processed simulations, are shown in Appendix B. The parameters are non-degenerate and the credible regions of parameter space are therefore well defined. We marginalize over each parameter in turn by collapsing the likelihood matrix and computing new credible interval bounds. Both parameters increase smoothly with redshift, as shown in Fig. 15. The average flux decreases steadily with increasing redshift over $4.9 < z < 5.9$. While the UVB in simulations is explicitly tuned to match the mean flux, the mean flux recovered after post-processing the lines of sight is slightly lower than measured from observations. This most likely reflects a difference in the clustering of transmission in the simulations: if the transmission occurs in isolated spikes, the flux is more likely to go undetected after observational errors are taken into account (see e.g. Chardin et al. 2018).

This decrease in average flux with redshift is accompanied by a smooth increase in the skewness of the distribution until $z \sim 5.9$, followed by a tentative decrease at $5.9 < z < 6.1$. This correspond to an increasingly non-normal distribution of transmission at higher redshift. The decrease in skewness in the highest redshift bin reflects the fact that transparent lines of sight are not found at $z > 5.9$. However, no current spectrograph is capable of measuring opacities larger than $\tau \sim 8$, and using a lognormal form for residual flux distribution becomes increasingly less appropriate.

The Sherwood simulation and the model of Keating et al. (2017) shows a very modest increase with redshift, while only the model from Chardin et al. (2017) is displaying sufficient non-Gaussianity. The highest redshift bin $5.9 < z < 6.1$ is the only one where the Sherwood and Keating et al. (2015) simulations match the data, as the excess in skewness seen at $5.3 < z < 5.9$ in the data seems to be absent. Table 5 gives the most likely values for $\overline{F}$ and s at all redshifts and for all post-processed models. The most likely intrinsic distribution of opacities is plotted in Fig. 8 as a dashed line.

7 DISCUSSION

Our results confirm the long-lasting inhomogeneity of the IGM opacity to Lyman-α after the end of reionization. This inhomogeneity is seen to persist as late at $z = 5.3$, which is perplexing since photon percolation is predicted to have happened by that redshift by all theoretical models. We confirm the increasing scatter of Lyman-α opacity with higher redshift first reported by Becker et al. (2015b). In fact, previous studies may have been too optimistic in their treatments of non-detections of Lyman-α flux. With a large enough sample of lines of sight, we found that the distribution of residual fluxes was aptly described by a lognormal distribution and were able to incorporate constraints from non-detections in a fully consistent way. This choice of distribution is purely empirical, as the lognormal is the most common distributing function for variables which are constrained to be positive, such as flux. Using this parametrization, we extract a linear increase in mean opacity from $\overline{\tau}_{\text{Ly}\alpha} \sim 1.8$ at $z = 5.0$ to $\overline{\tau}_{\text{Ly}\alpha} \sim 3.8$ at $z = 6.0$. It is remarkable, but perhaps not surprising, that all the numerical simulations we confronted with the data required a strongly redshift-dependent rescaling of the source emissivity to match this smooth increase in opacity.

Another perhaps surprising outcome of our analysis is the lack of binning-scale dependence (Section 4.2, Fig. 10). The CDF of effective opacity computed with binning scales of 30, 50, and 70 cMpc h^{-1} are consistent with each other according to a two-sided KS test, with only the case with 10 cMpc h^{-1} showing deviation. Different processes proposed to drive opacity fluctuations act on different scales; generally speaking, the coherence scales of density and temperature fluctuations are shorter than those of UVB fluctuations (e.g. Becker et al. 2015b; Davies & Furlanetto 2016; Keating et al. 2017). The models currently included in our analysis only span box sizes of 20 cMpc h^{-1} across, which is insufficient for such an analysis at the present time. Explicitly testing this scale dependence however provides a promising avenue for future work.

[lviii]The main caveat in this study, which is also related to a weak point in current numerical simulations, lies in the difficulty of ensuring we are measuring the opacity of the IGM itself as opposed to intervening DLA systems and other absorbers that are not part

Table 5. Most likely intrinsic parameter values with 68 per cent credible intervals, following equations (3) and (4). Best-fitting values are marginalized over the other parameter. The errors on simulations are approximately ±0.033 for s and ±0.0023 for $\overline{F}$, corresponding to the resolution down to which the bayesian likelihood analysis was run. Although the emissivity in the simulations is tuned to match $\overline{F}$, small differences emerge due to the random nature of the forward modelling. The values listed for $\overline{F}_{\rm fit}$ here are the values derived from the maximum-likelihood fit to the lognormal distribution, not the ones extracted directly from the $\tau_{\rm eff}$ measurements, which are more robust and given in Table 4.

Δz	$\overline{F}_{\rm fit}$	$s_{\rm fit}$	$\overline{F}_{\rm Chardin}$	$s_{\rm Chardin}$	$\overline{F}_{\rm Keating}$	$s_{\rm Keating}$	$\overline{F}_{\rm Sherwood}$	$s_{\rm Sherwood}$
4.9–5.1	$0.146^{+0.023}_{-0.014}$	$1.15^{+0.30}_{-0.15}$	N/A	N/A	0.138	0.84	0.141	0.67
5.1–5.3	$0.112^{+0.007}_{-0.006}$	$1.34^{+0.20}_{-0.13}$	N/A	N/A	0.110	1.07	0.105	0.87
5.3–5.5	$0.094^{+0.012}_{-0.009}$	$2.21^{+0.33}_{-0.27}$	0.089	1.82	0.087	0.80	0.086	0.67
5.5–5.7	$0.063^{+0.016}_{-0.010}$	$3.6^{+2.4}_{-1.3}$	0.062	3.02	0.057	1.50	0.057	1.00
5.7–5.9	$0.036^{+0.010}_{-0.005}$	$4.5^{+3.0}_{-1.2}$	0.038	5.70	0.035	1.82	0.030	1.44
5.9–6.1	$0.007^{+0.003}_{-0.002}$	$2.6^{+2.7}_{-0.9}$	N/A	N/A	0.007	2.80	0.005	1.78

of the optically thin IGM. Finding these systems via the accompanying decrement to Lyman-α flux is very difficult at the redshifts studied here given how strongly the Lyman-α forest is already absorbed. We have explicitly removed all systems displaying C IV absorption in the quasar continuum redward of Lyman-α. However, weakly ionized transitions such as Mg and O require far red and IR spectra of reasonably high resolution and S/N, which we lack in many cases. Systems containing these ions often do not show C in absorption, and their numbers could potentially be increasing at high redshift (Becker et al. 2006; Bosman et al. 2017; Codoreanu et al. 2017). Nevertheless, one would need to discard the measurements obtained along the most opaque 30 per cent of our sample in order for the remaining lines of sight to match the Sherwood smooth-UVB prediction at $5.1 < z < 5.3$, and this fraction rises to 60 per cent of the sample at $5.7 < z < 5.9$. A smooth UVB at those redshifts is therefore confidently ruled out even in the presence of this caveat. At the same time, recent research has highlighted the crucial importance of including self-shielding effects for numerical simulations of reionization (e.g. Madau 2017). Bridging this gap can therefore be done from different angles, as improved surveys will constrain the occurrence rates of low-mass systems in the epoch of reionization to enable better removal, and numerical simulations become more refined.

8 SUMMARY

We have assembled a sample of 62 optical spectra of quasars with $z_{\rm source} \geqslant 5.7$ in order to measure the distribution of IGM Lyman-α transmission over $5 < z < 6$. These objects consist of 13 SDSS-discovered quasars, 10 quasars from DES–VHS, 4 from the SHELLQs survey, 13 from online telescope archives, 19 from previous similar studies, and 3 new spectra. The data originate from a total of 10 different optical spectrographs and have been collected over the course of the last 11 yr. We use this unprecedented sample of high-z quasars to improve the measurements of residual Lyman-α transmission of Fan et al. (2006) and Becker et al. (2015b). The large variance in opacity among lines of sight has previously been shown to be incompatible with a uniform UVB. At the same time, unexpectedly large longitudinal correlations in opacity of up to 110 cMpc h^{-1} at $z > 5.5$ mean that only a dramatic increase in number of background sources – and not a finer sampling – can aptly quantify cosmic variance (Becker et al. 2015b).

We confirm the existence of a long-lasting inhomogeneity in the Lyman-α opacity of the IGM at $5.5 < z < 5.9$, but also detect a significant departure from the opacity distribution expected for a spatially uniform UVB and temperature–density relation down to $z \sim 5.2$. If the data genuinely reflect large fluctuations in intergalactic opacity at such low redshifts, it may present a significant further challenge to models of reionization the post-reionization IGM. We also extend our study to $5.9 < z < 6.1$, finding increased opacity.

In order to deal with the disparate data quality in our sample and present limits in a transparent way, we then introduce a second bound on the CDF which is 'maximally pessimistic', i.e. non-detections are taken to mean that $\tau \to \infty$. This allows us to incorporate moderately deep data while being confident that the 'true' CDF lies in-between these two bounds; in other words our results present the region permitted by current data.

We further explore an empirical lognormal fit to the CDF, which is characterized by a mean opacity and a skewness. Both detections and non-detections are used to constrain the underlying shape of the opacity distribution. We find a linear increase in mean Lyman-α opacity with redshift from $\overline{\tau}_{\rm Ly\alpha} \sim 2.0$ at $z = 5.0$ to $\overline{\tau}_{\rm Ly\alpha} \sim 4.9$ at $z = 6.0$, accompanied by a smooth increase in skewness.

Altering the comoving size of the binning window produces only subtle effects on the distribution between the l= 30, 50, and 70 cMpc h^{-1} cases at any redshift. A binning with $l = 10$ cMpc h^{-1} significantly broadens the distribution of effective optical depths at $z < 5.7$. We also vary the length of the excluded 'proximity region' which is affected by the source quasar itself, finding no effect at any redshift on the statistical distribution of transmitted flux as long as $\lambda_{\rm end,\,prox} < 1180$ Å is adopted. The traditionally used value of $\lambda_{\rm end,\,prox}$= 1176 Å is thus valid and we do not expect significant contamination from the quasar proximity zones.

We compare our final results with outputs from three different published numerical models: the Sherwood simulation, which uses a spatially uniform UVB (Bolton et al. 2017); the radiative transfer post-processed simulation of Keating et al. (2017), which models temperature fluctuations arising from differences in the timing of reionization; and a model including rare, bright sources from Chardin et al. (2017). Echoing previous works, we find that the data strongly disfavour the uniform UVB model and the radiation transfer model in their current forms. The rare sources model is marginally consistent with data at $z > 5.7$ but not at $5.5 < z < 5.7$. More work may be required to determine whether variations of these models may be more consistent with the present data.

In light of these results, the extreme scatter of Lyman-α opacity at the tail end of reionization remains a perplexing puzzle.

ACKNOWLEDGEMENTS

The authors thank the anonymous reviewer for useful and pertinent comments pointing out multiple avenues for future work. SEIB thanks Alberto Rorai and Tricia Larsen for many productive discussions. The authors are grateful to Laura Keating, Jonathan Chardin,

and Girish Kulkarni for kindly sharing the outputs of the radiative transfer, rare sources, and Sherwood simulations, respectively. The authors also thank Ian McGreer for agreeing to share reduced spectra from his 2015 paper.

This research has made use of the KOA, which is operated by the W. M. Keck Observatory and the NASA Exoplanet Science Institute, under contract with the National Aeronautics and Space Administration. Based on data obtained from the ESO Science Archive Facility. This work is based in part on observations made with ESO Telescopes at the La Silla Paranal Observatory under program IDs 084.A-0390, 096.A-0095, and 096.A-0411.

This paper used data obtained with the MODS spectrographs built with funding from NSF grant AST-9987045 and the NSF Telescope System Instrumentation Program, with additional funds from the Ohio Board of Regents and the Ohio State University Office of Research.

Some of the data presented herein were obtained at the W. M. Keck Observatory, which is operated as a scientific partnership among the California Institute of Technology, the University of California, and the National Aeronautics and Space Administration. The Observatory was made possible by the generous financial support of the W. M. Keck Foundation. The authors wish to recognize and acknowledge the very significant cultural role and reverence that the summit of Maunakea has always had within the indigenous Hawaiian community. We are most fortunate to have the opportunity to conduct observations from this mountain.

SEIB acknowledges funding from the European Research Council (ERC) under the European Union's Horizon 2020 research and innovation programme (grant agreement No 669253), as well as a Graduate Studentship from the Science and Technology Funding Coucil (STFC). Support by the ERC Advanced Grant Emergence - 32056 is gratefully acknowledged. XF acknowledges support from the U.S. NSF grant AST 15-15115. LJ acknowledges support from the National Key R&D Program of China (2016YFA0400703) and from the National Science Foundation of China (grant 11533001). GB acknowledges support from the NSF under grant AST-1615814.

The Sherwood simulation was performed with supercomputer time awarded by the Partnership for Advanced Computing in Europe 8th call. This project also made use of the DiRAC High Performance Computing System and the COSMOS shared memory service at the University of Cambridge. These are operated on behalf of the STFC DiRAC HPC facility. This equipment is funded by BIS National E-infrastructure capital grant ST/J005673/1 and STFC grants ST/H008586/1 and ST/K00333X/1.

REFERENCES

Andrae R., 2010, preprint (arXiv:1009.2755)
Barlow R., 1989, Probability and Confidence, in Statistics: A Guide to the Use of Statistical Methods in the Physical Sciences. Wiley, New York, p. 125.
Becker G. D., Bolton J. S., 2013, MNRAS, 436, 1023
Becker G. D., Sargent W. L. W., Rauch M., Simcoe R. A., 2006, ApJ, 640, 69
Becker G. D., Sargent W. L. W., Rauch M., Carswell R. F., 2012, ApJ, 744, 91
Becker G. D., Bolton J. S., Lidz A., 2015a, PASA, 32, e045
Becker G. D., Bolton J. S., Madau P., Pettini M., Ryan-Weber E. V., Venemans B., 2015b, MNRAS, 447, 3402
Bolton J. S., Puchwein E., Sijacki D., Haehnelt M. G., Kim T.-S., Meiksin A., Regan J. A., Viel M., 2017, MNRAS, 464, 897
Bosman S. E. I., Becker G. D., Haehnelt M. G., Hewett P. C., McMahon R. G., Mortlock D. J., Simpson C., Venemans B. P., 2017, MNRAS, 470, 1919
Buzzoni B. et al., 1984, The Messenger, 38, 9
Carilli C. L. et al., 2010, ApJ, 714, 834
Carnall A. C. et al., 2015, MNRAS, 451, L16
Chardin J., Haehnelt M. G., Aubert D., Puchwein E., 2015, MNRAS, 453, 2943
Chardin J., Puchwein E., Haehnelt M. G., 2017, MNRAS, 465, 3429
Chardin J., Haehnelt M. G., Bosman S. E. I., Puchwein E., 2018, MNRAS, 473, 765
Chen S.-F. S. et al., 2016, ApJ, 850, 188
Codoreanu A., Ryan-Weber E. V., Crighton N. H. M., Becker G., Pettini M., Madau P., Venemans B., 2017, MNRAS, 472, 1023
D'Aloisio A., McQuinn M., Trac H. 2015, ApJ, 813, L38
D'Odorico V. et al., 2013, MNRAS, 435, 1198
Davies F. B., Furlanetto S. R., 2016, MNRAS, 460, 1328
Davies F. B., Hennawi J. F., Eilers A.-C., Lukić Z., 2017, ApJ, 855, 106
Eilers A.-C., Davies F. B., Hennawi J. F., Prochaska J. X., Lukic Z., Mazzucchelli C., 2017, ApJ, 840, 24
Fan X. et al., 1999, AJ, 118, 1
Fan X. et al., 2000, AJ, 120, 1167
Fan X. et al., 2001, AJ, 122, 2833
Fan X. et al., 2003, AJ, 125, 1649
Fan X. et al., 2004, AJ, 128, 515
Fan X. et al., 2006, AJ, 132, 117
Fukugita M., Ichikawa T., Gunn J. E., Doi M., Shimasaku K., Schneider D. P., 1996, AJ, 111, 1748
Goto T., 2006, MNRAS, 371, 769
Gunn J. E., Peterson B. A., 1965, ApJ, 142, 1633
Haardt F., Madau P., 2012, ApJ, 746, 125
Hogg D. W., Finkbeiner D. P., Schlegel D. J., Gunn J. E., 2001, AJ, 122, 2129
Hook I. M., Jørgensen I., Allington-Smith J. R., Davies R. L., Metcalfe N., Murowinski R. G., Crampton D., 2004, PASP, 116, 425
Horne K., 1986, PASP, 98, 609
Jiang L., Fan X., Vestergaard M., Kurk J. D., Walter F., Kelly C., Strauss M. A., 2007, AJ, 134, 1150
Jiang L. et al., 2008, AJ, 135, 1057
Jiang L. et al., 2009, AJ, 138, 305
Jiang L., McGreer I. D., Fan X., Bian F., Cai Z., Clément B., Wang R., Fan Z., 2015, AJ, 149, 188
Jiang L. et al., 2016, ApJ, 833, 222
Kaiser N. et al., 2010, in Stepp L. M., Gilmozzi R., Hall H. J. eds, Proc. SPIE, Vol. 7733, Ground-based and Airborne Telescopes III, SPIE, Bellingham, p. 77330E
Kashikawa N. et al., 2002, PASJ, 54, 819
Keating L. C., Haehnelt M. G., Cantalupo S., Puchwein E., 2015, MNRAS, 454, 681
Keating L. C., Puchwein E., Haehnelt M. G., 2017, MNRAS, 477, 5501
Kelson D. D., 2003, PASP, 115, 688
KOA. 2017, W. M. Keck Observatory Archive, https://koa.ipac.caltech.edu/cgi-bin/KOA/nph-KOAlogin
Kolmogorov A., 1933, Inst. Ital. Attuari Giorn., 4, 83
Lawrence A. et al., 2007, MNRAS, 379, 1599
Lidz A., Oh S. P., Furlanetto S. R., 2006, ApJ, 639, L47
Madau P., 2017, ApJ, 851, 50
Marshall J. L. et al., 2008, in McLean I. S., Casali M. M., eds, Proc. SPIE, Vol. 7014, Ground-based and Airborne Instrumentation for Astronomy II, SPIE, Bellingham, p. 701454
Matsuoka Y. et al., 2016, ApJ, 828, 26
Matsuoka Y. et al., 2017, PASJ, 70, S35
McGreer I. D., Mesinger A., D'Odorico V., 2015, MNRAS, 447, 499
McGreer I. D., Mesinger A., Fan X., 2011, MNRAS, 415, 3237
McMahon R. G., Banerji M., Gonzalez E., Koposov S. E., Bejar V. J., Lodieu N., Rebolo R., VHS Collaboration, 2013, The Messenger, 154, 35
McQuinn M., Hernquist L., Lidz A., Zaldarriaga M., 2011, MNRAS, 415, 977
Mesinger A., 2010, MNRAS, 407, 1328

Miyazaki S. et al., 2012, in McLean I. S., Ramsay S. K., Takami H. eds, Proc. SPIE, Vol. 8446, Ground-based and Airborne Instrumentation for Astronomy IV, SPIE, Bellingham, p. 84460Z
Morganson E. et al., 2012, AJ, 143, 142
Mortlock D. J. et al., 2009, A&A, 505, 97
Mortlock D. J. et al., 2011, Nature, 474, 616
Planck Collaboration XIII et al. 2016, A&A, 594, A13
Pogge R. W. et al., 2012, in McLean I. S., Ramsay S. K., Takami H. eds, Proc. SPIE, Vol. 8446, Ground-based and Airborne Instrumentation for Astronomy IV, SPIE, Bellingham, p. 84460G
Reed S. L. et al., 2015, MNRAS, 454, 3952
Reed S. L. et al., 2017, MNRAS, 468, 4702
Ryan-Weber E. V., Pettini M., Madau P., Zych B. J., 2009, MNRAS, 395, 1476
Sheinis A. I., Bolte M., Epps H. W., Kibrick R. I., Miller J. S., Radovan M. V., Bigelow B. C., Sutin B. M., 2002, PASP, 114, 851
Simcoe R. A. et al., 2011, ApJ, 743, 21
Songaila A., 2004, AJ, 127, 2598
Springel V., 2005, MNRAS, 364, 1105
The Dark Energy Survey Collaboration, 2005, preprint (astro-ph/0510346)
Venemans B. P., McMahon R. G., Warren S. J., Gonzalez-Solares E. A., Hewett P. C., Mortlock D. J., Dye S., Sharp R. G., 2007, MNRAS, 376, L76
Venemans B. P. et al., 2013, ApJ, 779, 24
Venemans B. P. et al., 2015, MNRAS, 453, 2259
Vernet J. et al., 2011, A&A, 536, A105
Wang F. et al., 2016, ApJ, 819, 24
Willott C. J. et al., 2007, AJ, 134, 2435
Willott C. J. et al., 2009, AJ, 137, 3541
Willott C. J. et al., 2010, AJ, 139, 906
Wu X.-B. et al., 2015, Nature, 518, 512
Wyithe J. S. B., Bolton J. S., 2011, MNRAS, 412, 1926
York D. G. et al., 2000, AJ, 120, 1579

SUPPORTING INFORMATION

Supplementary data are available at *MNRAS* online.

alldata_silver.ods

Please note: Oxford University Press is not responsible for the content or functionality of any supporting materials supplied by the authors. Any queries (other than missing material) should be directed to the corresponding author for the article.

APPENDIX A: MOSAIC OF QUASAR CATALOGUE

In Figs A1 and A2, we plot all the $z > 5.7$ quasar spectra used in this work in a common format. The spectra are normalized by dividing the flux by a best-fitting PL. Wavelengths are divided by $z_{\rm source} + 1$ to bring the spectra into the rest frame. The *y*-axis is calibrated so that it spans the range $0 \rightarrow 5$ ×continuum for each quasar. We do not bin the spectra in order to reflect the diversity of data qualities present in the sample. Error arrays are shown in red.

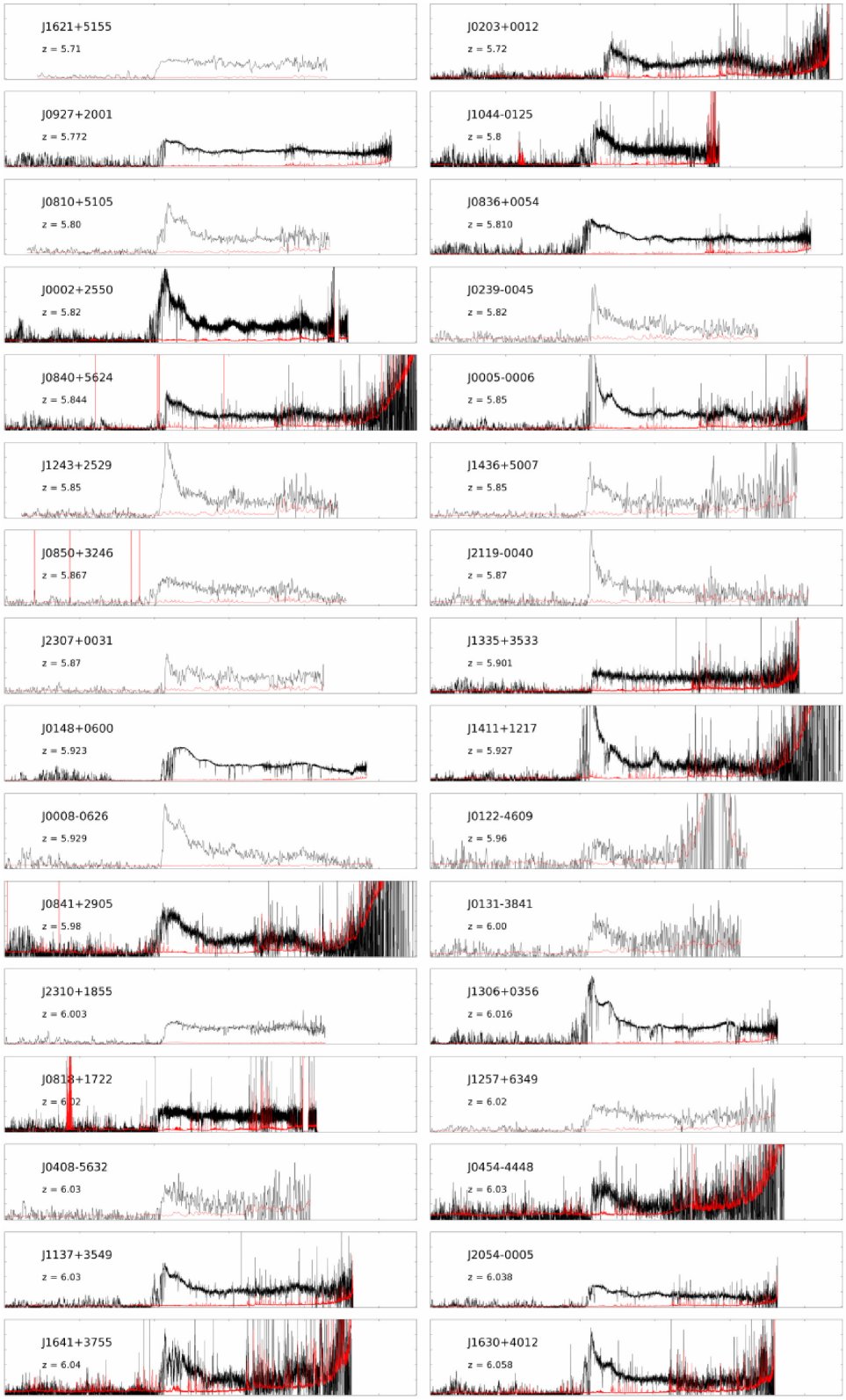

Figure A1. First half of the quasar catalogue. The origin of each spectrum and the instruments used are listed in Table1. Wavelength runs from 1000 to 1550 Å and the fluxes have been normalized by dividing by the best-fitting PL to the continuum.

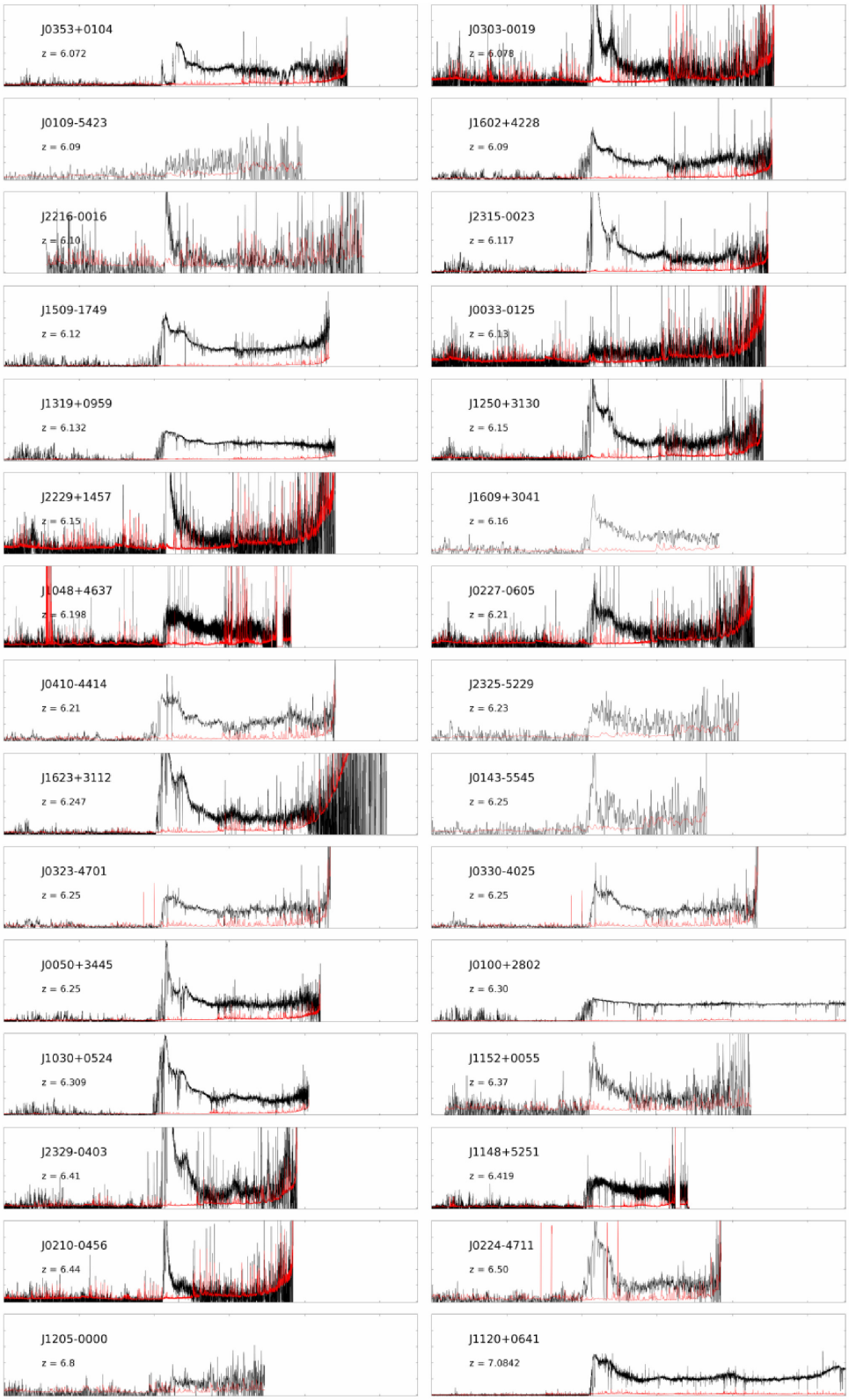

Figure A2. Second half of the quasar catalogue. Data are as in Fig. B1.

APPENDIX B: POSTERIOR DISTRIBUTION OF $\overline{F}$ AND s

In Fig. B1, we show the posterior distribution in $\overline{F}$–s parameter space for both the data and best-fitting values for the post-processed simulations. The results given throughout the paper are marginalized over either one of the two parameters. We plot the skewness on a logarithmic scale to emphasize the fact that the distribution is consistent with being 'maximally skewed' at $z > 5.9$, which following equation (3) corresponds to an exponential distribution tending to infinity at $F = 0$. The 68 per cent and 90 per cent credible intervals are shown as concentric contours. The coloured thick lines correspond to simulations from Chardin et al. (2017, orange), Keating et al. (2017, red), and Bolton et al. (2017, blue), post-processed as described in Section 5.1.

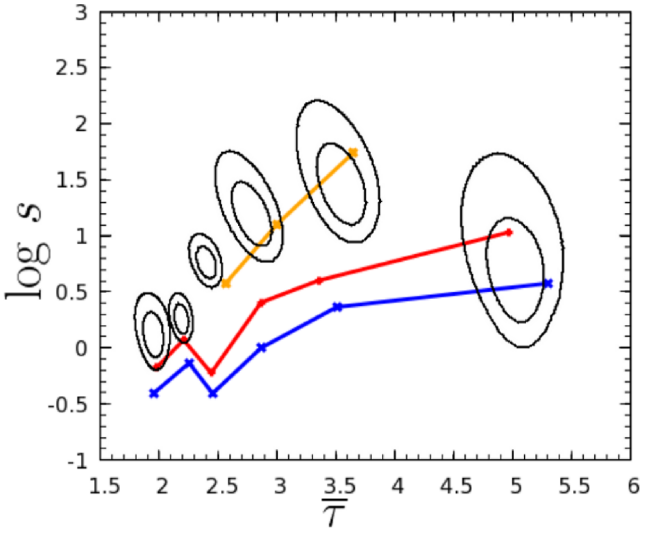

Figure B1. Posterior distributions on the skewness s and mean opacity $\overline{\tau} = -\log \overline{F}$ of Lyman-α transmission. Different contours correspond to redshift ranges of $\Delta z = 0.2$ beginning at $z = 4.9$, 5.1, 5.3, 5.5, 5.7, and 5.9, following the direction indicated by the arrow. The coloured thick lines correspond to simulations from Chardin et al. (2017, orange), Keating et al. (2017, red), and Bolton et al. (2017, blue), post-processed to mimic observational data as described in Section 5.1.

This paper has been typeset from a TEX/LATEX file prepared by the author.